# SPIN-ORBIT TORQUE DRIVEN MAGNETIZATION DYNAMICS IN (GA,MN)AS AND (GA,MN)(AS,P) DILUTE MAGNETIC SEMICONDUCTORS

A Thesis

by

ERIN KATHLEEN VEHSTEDT

Submitted to the Office of Graduate and Professional Studies of
Texas A&M University
in partial fulfillment of the requirements for the degree of

MASTER OF SCIENCE

| | |
|---|---|
| Chair of Committee, | Jairo Sinova |
| Committee Members, | Harlan Rusty Harris |
| | Joseph H. Ross Jr. |
| Head of Department, | George R. Welch |

August 2014

Major Subject: Physics

# ABSTRACT

Spintronics-based technologies are poised to leapfrog the current limitations on the scaling, speed, and power consumption of electronic devices. Conventional devices rely on complex structures and magnetic-field-based switching to manipulate data. In order to overcome these limits, new methods must be developed to reliably transmit and store data more efficiently. The understanding and manipulation of magnetic domain walls (DWs) may play a pivotal role in the development of new non-volatile and down-scalable logic and memory devices.

This thesis investigates current-induced magnetization dynamics and control mechanisms in the ideal ferromagnetic semiconductors Phosphorus-doped Gallium Manganese Arsenide (Ga,Mn)(As,P) and Gallium Manganese Arsenide (Ga,Mn)As. In spin-orbit (SO) coupled materials with broken inversion symmetry, unpolarized electric fields provide a means to control magnetization orientation via the inverse spin-galvanic effect (ISGE). The ISGE generates a non-equilibrium spin-accumulation which can exert a torque on a magnetization if the spins are generated in (or injected into) a ferromagnetic material. This so-called current-induced spin-orbit torque (SOT) is calculated for a broad range of experimental parameters and compared with previous measurements.

The study also assess the viability of using SOTs to control DW motion in semiconductor micro-structures. Typically, DW mobility is divided into steady and precession motion regimes with different mobilities, separated by the so-called Walker breakdown (WB). By manipulating the magnetic anisotropy of (Ga,Mn)(As,P) using piezoelectric strain, these experiments investigate the potential of strain to shift the WB, establishing strain-modified DW mobility as tool for electrically controlled DW motion.

ACKNOWLEDGMENTS

I am grateful for the support and guidance I received from the many collaborators with whom I worked on this project. At Texas A&M: my advisor, Prof. Jairo Sinova, who made it possible for me to work on both the theory and experimental aspect of the study. Prof. Helmut G. Katzgraber and his former students Dr. Ruben Andrist and Dr. Juan Carlos Anderson who provided answers to endless queries as I migrated from running simulations locally to using high performance supercomputers. Prof. Tomas Jungwirth, Dr. Liviu P. Zárbo, and Dr. Karel Výborý at the Institute of Physics, ASCR v.v.i. with whom I worked on the theoretical studies, as well as Xavi Marti with whom I shared many helpful discussions. Dr. Joerg Wunderlich, Dr. Elisa De Ranieri, and Dr. Pierre Roy at the Hitachi Cambridge Laboratory with whom I conducted the domain wall experiments. At the Microelectronics Research Centre, University of Cambridge: Prof. Andrew J. Ferguson, Dr. Hidekazu Kurebayashi, and Dr. Dong Fang, for continual discussions and their work on spin-orbit driven ferromagnetic resonance; Dr. Andrew C. Irvine, Dr. Dominik Heiss, and Dr. Chiara Ciccarelli who assisted me with fabrication; and a special thanks to Radoslav Chakalov for managing the cleanroom superbly.

I would also like to acknowledge the support of the US National Science Foundation, NSF TAMUS LSAMP BTD award 1026774, the Texas A&M University Office of Graduate Studies, and the EU Marie Curie Program award FP7-215368 SemiSpinNet for providing funding. I am grateful to my hosts, Prof. Jungwirth at the Institute of Physics, Academy of Sciences of the Czech Republic v.v.i., Prague, Czech Republic and Dr. David Williams at the Hitachi Cambridge Laboratory, Cambridge, United Kingdom. The computational work used HPC resources provided by the Extreme Science and Engineering Discovery Environment (XSEDE), which is supported by National Science Foundation grant number ACI-1053575, and by the Texas Advanced Computing Center (TACC) at The University of Texas at Austin.

Finally, to the many people whose names are not included here who have helped me along the way, you have not been forgotten, but to include all of you here would take up another thesis.

TABLE OF CONTENTS

Page

Page

LIST OF TABLES

TABLE Page

LIST OF FIGURES

FIGURE Page

FIGURE Page

# 1 INTRODUCTION

The proliferation of personal electronic devices highlights both the incredible technological advances and the immediate need to find for advances in low-energy alternatives such as spintronics. Consumer electronics, e.g. computers and smart phones, are largely comprised of logic and memory elements. One of the earliest impacts of spintronics technologies on consumer devices was the use of  in magnetic hard drives. The use of these metal-based spintronics revolutionized personal information storage.

In modern electronics, logic circuits are controlled using electrical currents, and are typically responsible for Boolean operations. On the contrary, magnetoresistive random access memory (MRAM) employs arrays of thin-film multilayers where data storage and processing are performed by switching the orientation of an individual magnetic layer in each stack; power consumption is determined by the critical current required to switch each MRAM bit. Conventional MRAM uses magnetic-field-based switching, necessitating large critical currents and limiting scalability. The next generation of spin-based memory came in the recently-commercialized spin-transfer torque magnetic random access memory (STT-MRAM), which uses spin-transfer torque (STT) driven magnetization switching. This work goes one step further to explore the possibility of using spin-orbit torques (SOTs) generated via the inverse spin-galvanic effect (ISGE) to control magnetization orientation in dilute magnetic semiconductors.

Advances in this area herald the potential of spintroinics to revolutionize the the industry once more. By establishing SOT as a viable control mechanism, this work represents an important step towards the integration of nonvolatile memory and logic elements into a single device architecture. Thus, dramatically reducing stand-by power consumption while improving interconnection times, and opening the door to a whole new class of faster, more energy efficient, personal electronic devices.

# 2 BACKGROUND

This chapter discusses the theoretical and experimental basis of the techniques used in this study of SOTs in dilute magnetic semiconductors (DMSs) and its application to current-induced domain wall (DW) motion. In Section 2.1 the structural properties of the quintessential DMSs (Ga,Mn)As and (Ga,Mn)(As,P) are reviewed, along with some details of their growth. Their magnetic properties and the role of anisotropy are discussed in Section 2.3, followed by the spin-orbit interaction (SOI) in Section 2.2.The chapter concludes with an introduction to the concept of current-induced SOT, Section 2.4, and its importance in realizing fully-electric control of DW motion.

## 2.1 Properties of Dilute Magnetic Semiconductors

### 2.1.1 Crystal structure

These studies focus on doped GaAs, one of the most well-characterized III-V semiconductors (along with InAs. [1, 2] GaAs forms a zinc-blende crystal structrure and can be grown into large single crystals by several methods. This, combined with its wide direct band gap and strong electrical insulation, has made GaAs a common substrate for certain electronic applications, e.g. mobile phone circuitry. [3]. This thesis focuses on the A-site substituted (Ga,Mn)As and the AB-substituted (Ga,Mn)(As,P) families of materials. Both the single and co-doped materials retain their parent crystal structure, undergoing a change in uniaxial strain with Mn doping.

### 2.1.2 Doping

The addition of magnetic impurities (Mn) to GaAs posed some difficulties in early research, as Mn substitution (for Ga) could not exceed a fraction of a percent with

traditional GaAs growth techniques. The advent of molecular beam epitaxy (MBE) allowed super-soluble concentrations of (Ga,Mn)As to be grown, with sufficient Mn to induce ferromagnetism. Initially this technique produced poor-quality crystals, as normal MBE growth temperatures (600 °C) allow Mn to migrate to the surface. [4] It was later discovered that high quality single crystalline (Ga,Mn)As could be grown using low-temperature molecular beam epitaxy (LT - MBE) in conjunction with post-growth annealing, the techniques used for the materials discussed here. A detailed analysis of the wafer growth process can be found in ref. [5]

A key improvement of this project is the use of secondary phosphorus doping in (Ga,Mn)As, which serves two purposes. First, it results in very high quality growth with almost no pinning centers (which prevent DWs from traveling), making it superior to previous material for the study of DW motion. Second, and more importantly, the addition of significant ( 10%) phosphorus changes the sign of the growth strain, and brings the magnetic easy-axis out of plane. This proves particularly useful for these measurements as it enables the use of the polar magneto-optic Kerr effect (MOKE) to visualize the magnetization orientation in the sample.

### 2.1.3 Ferromagnetism

Both (Ga,Mn)As and (Ga,Mn)(As,P) are dilute semiconductors, which, when optimally-doped, can be well-described as uniform ferromagnets. For very low doping, less than 0.1%, (Ga,Mn)As is an insulting paramagnet. The onset of ferromagnetism in (Ga,Mn)As occurs near 1% Mn doping, above which the separation of Mn sites is small enough to allow for carrier (hole)-mediated ferromagnetic interactions between local Mn moments. [6–10]. The exact nature of this transition has been the source of much debate, and extends beyond the scope of this work. Above the ferromagnetic threshold, additional doping resulting in reduced disorder (by increasing the regularity of Mn dopant sites), until Mn concentrations reach  10%. Successful crystal growth for dopings above $10 - 13\%$ is extremely difficult.

### 2.1.4 Curie temperature

In the range of interest for this work, $3\% - 9\%$ A-site doping, higher Mn concentrations are associated with improved crystal growth quality and increased Curie temperature. One of the primary aims of research in (Ga,Mn)As and other DMSs is to achieve room temperature ferromagnetism. Initial (Ga,Mn)As samples typically attained $T_C \approx 60$ K [2], but improvements in growth techniques such as LT - MBE have lead to records up to 110 K which can be further improved by the use of post-growth annealing regimens, achieving record Curie temperatures of 190 K for 13% Mn doping [11]. The success of these procedures is thought to be result of the reduction of interstitial manganese atoms which couple antiferromagnetically with on-site Mn and destroy ferromagnetism. [12–15]

## 2.2 Spin Orbit Interaction

The coupling of a carrier's spin degree of freedom ($\vec{\sigma}$) to its orbital motion (angular momentum, $\vec{L}$), is responsible for a wide range of interesting and exploitable material behaviors. This so-called SOI is a relativistic effect, whereby a moving charge (electron) bound to an atomic nucleus "sees" the nucleus as a bound positive charge in orbit. In the reference frame of the electron, this nuclear motion can be described as a "current" and generates an associated effective magnetic field

$$H = H_{free} + H_{SO} = \frac{p^2}{2m} + V + \frac{\hbar\sigma \cdot (\vec{p} \times \nabla V)}{4m^2c^2} \tag{2.1}$$

which includes both the free electron ($H_{free}$) and spin-orbit ($H_{SO}$) terms. Here $\vec{p}$ is the carrier momentum operator, $m$ is the mass, $\vec{\sigma}$ is the electron spin operator, and $\nabla V$ is the effective electric field generated by the orbital motion.[1] The consequences of this description are not immediately apparent. The SOI correction is small relative to the first term, and naively one might think they would not play an important

[1]Hole charge carriers are described using the total angular momentum, $\vec{J}$ rather than $\vec{\sigma}$

role when determining the band structure of a system. However, in materials with broken inversion symmetry, this interaction serves to lift the degeneracies between spin states.

The general form of the Hamiltonian shown in Eq. 2.1 has time-reversal symmetry. Kramers degeneracy notes that the conduction band energy is invariant under simultaneous $\vec{k} \rightarrow -\vec{k}$ and $\uparrow \rightarrow \downarrow$ transformations. [16] Thus, the symmetry of the band structure follows that of the Hamiltonian. For an inversion-symmetric Hamiltonian, E($\vec{k}$)=E(-$\vec{k}$); thus under the double transformation, $\vec{k}$ is unaffected, and we can conclude the spin states must be equivalent. For systems without inversion symmetry there are no such restrictions on energy under the single $\vec{k} \rightarrow -\vec{k}$, only the double transformation, so the spin states are not inherently degenerate. This is of particular importance to the studies discussed in this thesis, as SOTs could not exist without the ISGE which results as a response to an electric field applied to an inversion asymmetric system.

### 2.2.1 Inverse spin galvanic effect

The inverse spin galvanic effect (ISGE), also known as the Edelstein or kinetic magneto-electric effect [17] in two-dimensional electron gasses (2DEGs), is when a non-equalibrium spin polarization is generated in response to an applied electric field. In systems with strong spin-orbit coupling (SOC) and broken inversion symmetry (either in the Hamiltonian or the crystal), the addition of an applied electric field results in a redistribution of the carrier states on the Fermi surface and a perturbation of the carrier wave functions. [18–23] The resulting polarization can be treated as an effective magnetic field with then interacts with the magnetic moments within the system. (See Figs. 2.1, 2.2)

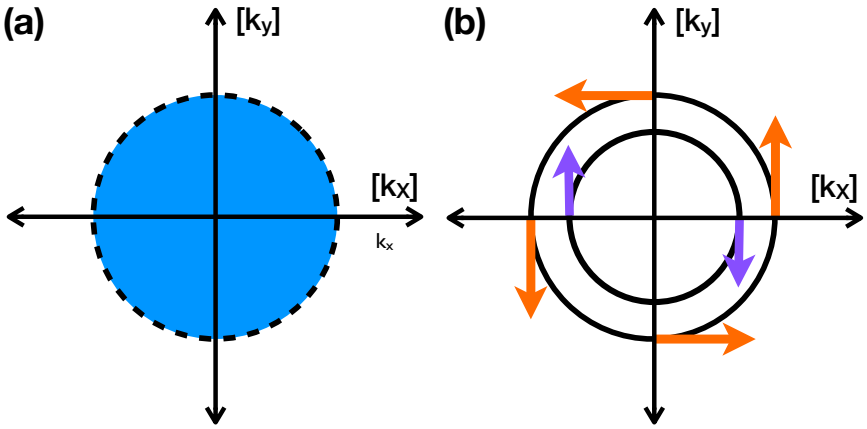


**Fig. 2.1.** Diagram of spin states (in k-space) and relative occupations in a 2DEG in the absence of an electric field

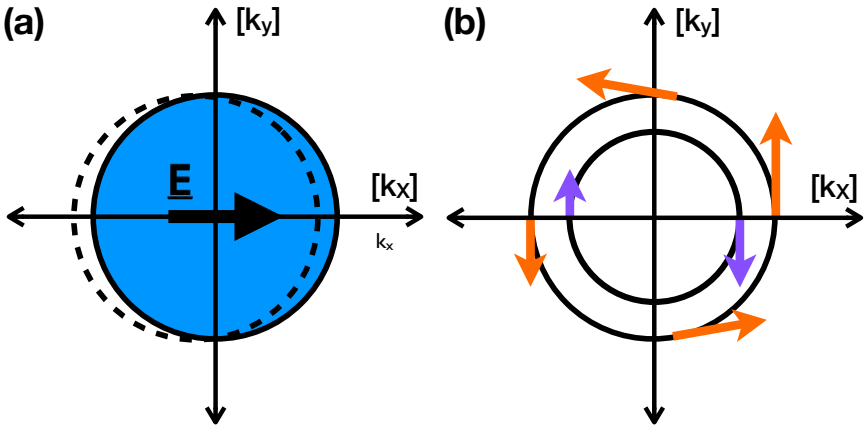


**Fig. 2.2.** Diagram of the redistribution of states as a result of the ISGE when an electric field is applied. Note that the sum of the carrier states is no longer zero, resulting in a non-equilibrium spin polarization.

### 2.2.2 Spin-orbit field symmetries

The SOI is typically divided into two sub-categories based on the symmetry of the spin-orbit (SO) fields. Dresselhaus spin-orbit coupling occurs in broken inversion symmetric crystals, e.g. GaMnAs, and can be described using the Dresselhaus Hamiltonian:

$$H_D = \gamma_0 \left[\sigma_x k_x (k_y^2 - k_z^2) + \sigma_y k_y (k_z^2 - k_x^2) + \sigma_z k_z (k_x^2 - k_y^2)\right], \tag{2.2}$$

which is proportional to $k^3$. The inclusion of crystal growth strain (at the substrate interface) produces an additional linear component, which results in a field symmetry in Fig. 2.3:

$$H_4 = C_4 \left[\sigma_x k_x (\epsilon_{yy} - \epsilon_{zz}) + \sigma_y k_y (\epsilon_{zz} - \epsilon_{xx}) + \sigma_z k_z (\epsilon_{xx} - \epsilon_{yy})\right]. \tag{2.3}$$

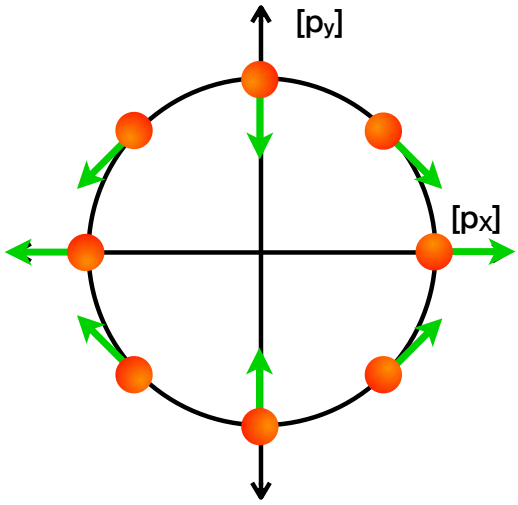


**Fig. 2.3.** Diagram of current-induced SOFs produced by Dresselhaus SOC (in k-space) for a zinc-blends crystal with positive growth strain

Rashba SOI, shows a completely different field symmetry as seen in Fig. 2.4, and follows the form:

$$H_R = \alpha(\vec{k} \times \hat{z}) \cdot \vec{\sigma}, \tag{2.4}$$

The axis of symmetry breaking (growth direction) is $\hat{z}$, and $\alpha$ is the Rashba coefficient used to model the relative strength of strain in the system. This can be mapped to the off-diagonal terms in the crystal strain tensor, which would be equivalent to an applied shear strain. [24–26]

$$H_R = C_3 \left[\sigma_x(\epsilon_{zz}k_z - \epsilon_{xy}k_y) + \sigma_y(\epsilon_{xy}k_x - \epsilon_{yz}k_z + \sigma_z(\epsilon_{yz}k_y - \epsilon_{zz}k_x)\right]. \tag{2.5}$$

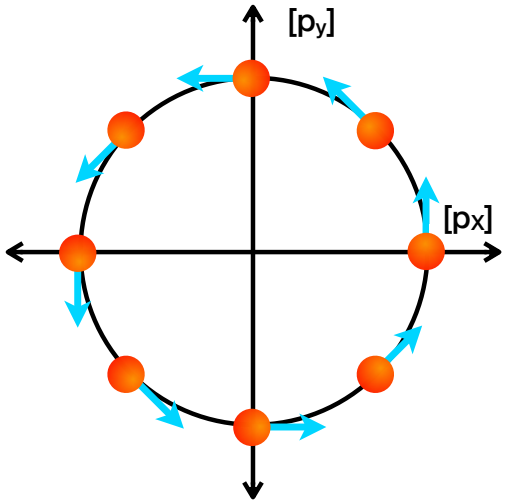


**Fig. 2.4.** Diagram of current-induced SOF symmetries resulting from Rashba SOC (in k-space) in a zinc-blends crystal with applied shear strain

## 2.3 Magnetic Anisotropy

Magnetic anisotropy is an important result of the SOI. It is the effect of the orientation of magnetic moment on magnetic properities; in crystalline systems this occurs when the symmetries result in lower energy state(s) where the magnetization is aligned along a particular orientation(s). A preferential direction is known as a magnetic 'easy axis', and materials with magnetic anisotropy are characterized by one (or more) easy axis (axes). [27]

In cubic systems, one can find cubic anisotropy where the preferred orientation is along the edges of the cube. Both bulk (Ga,Mn)As and (Ga,Mn)(As,P), exhibit cubic anisotropies. However, when grown as thin-films, the associated growth strain produces a strong uniaxial anisotropy due to lattice mismatch (in-plane for (Ga,Mn)As/GaAs, out of plane for (Ga,Mn)(As,P)/GaAs with sufficient phosphorus content). Rotating the magnetization away from this easy axis requires an additional energy cost, referred to as the anisotropy energy density. This can be measured via superconducting quantum interference device (SQUID) magnetometry, magneto-optical studies, and magneto-transport experiments.

Understanding and manipulating magnetic anisotropy is a primary goal of spintronics research, due to its role in magnetic memory and other device applications. Several avenues have been explored including non-magnetic doping (e.g. phosphorus), choice of substrate (lattice mismatch), and applied mechanical strain. Magnetic anisotropy is also highly temperature dependent, and applications of this are being explored in novel temperature-assisted MRAM devices not discussed here. [28] This work focuses on the use of piezo-electric actuators to induce shear strain in thin-film devices, as well as shape anisotropy as a result device patterning. The study of both (Ga,Mn)As and (Ga,Mn)(As,P) serves to compare compressive ((Ga,Mn)As) and tensile ((Ga,Mn)(As,P)) strained systems.

## 2.4 Spin Orbit Torque

### 2.4.1 Spin transfer torque

An early realization of electrically-controlled magnetization orientation was the discovery of STT [29]. Whereby a spin-polarized current is injected into a non-collinear ferromagnet, resulting in a torque upon the magnetization of the ferromagnet. This manipulation technique has been implemented in the emerging STT-MRAM, [30].

A simple theoretical picture of STT can be made by separating the non-equilibrium carrier spin density $\mathbf{s}$ and ferromagnetic magnetization $\mathbf{M}$ degrees of freedom. This separation can be justified when the difference in the timescales of the $\mathbf{s}$ and $\mathbf{M}$ dynamics. In DMSs such as (Ga,Mn)As, the saturation magnetization of the ferromagnet $\mathbf{M}$ is primarily due to Mn $d$-orbital local moments while the carrier states near the top of the valence band (or bottom of the conduction band) are dominated by As $p$-orbitals (or Ga $s$-orbitals). [31,32], which justifies the separation. The timescales can be evaluated for the non-equilibrium carrier spin polarization in the presence of the local magnetic moments exchange field as:

$$\frac{d\mathbf{s}}{dt} = \frac{J_{\mathrm{ex}} cS}{\hbar} \mathbf{s} \times \hat{\mathbf{M}} \,, \tag{2.6}$$

is $\tau_{\mathrm{ex}} = \hbar / J_{\mathrm{ex}} cS$, where $J_{\mathrm{ex}}$ is the exchange coupling constant of the local moments and carrier spins, $c$ is the local moment density, and $S$ is the magnitude of the local moment spin ($S_{\mathrm{Mn}} = 5/2$ for (Ga,Mn)As). For the case of the precession of the local moments in the exchange field of the non-equilibrium carrier spin polarization, we find

$$cS \frac{d\hat{\mathbf{M}}}{dt} = cS \frac{J_{\mathrm{ex}} |\mathbf{s}|}{\hbar} \hat{\mathbf{M}} \times \hat{\mathbf{s}} \,, \tag{2.7}$$

where $\hbar / J_{\mathrm{ex}} |\mathbf{s}|$ is the timescale. In typical STT experiments, $cS \gg |\mathbf{s}|$, and local moment dynamics are much slower than the non-equilibrium carrier spin dynamics.

[29, 33–36] Thus, we are well justified in separating the description of STT into two parts. First, we consider the fast dynamics, $\mathbf{s}$, and determine the steady-state component of the non-equilibrium carrier spin density, $\delta\mathbf{s}$. Next, the perturbation $\delta\mathbf{s}$ is introduced into Eq. (2.7) in order to infer the STTs acting on the magnetization $\mathbf{M}$ of the ferromagnet. We can describe the dynamics resulting from the injection of carriers polarized along $\hat{(}\mathbf{n}$ into a magnetic region aligned along $\mathbf{M}\hat{r}$ where $\hat{\mathbf{r}} \neq \hat{\mathbf{n}}$ by

$$\frac{d\delta\mathbf{s}}{dt} = \frac{1}{\tau_{ex}}\delta\mathbf{s} \times \hat{\mathbf{M}} + P\hat{\mathbf{n}} - \frac{\delta\mathbf{s}}{\tau_{\mathrm{s}}}. \tag{2.8}$$

The final term results from the finite spin-lifetime of the non-equilibrium carriers in the ferromagnetic region. By evaluating the limiting conditions of Eq. (2.8). [29, 33–36], we find two cases. The adiabatic (anti-damping) case occurs when the carrier spin lifetime $\tau_{\mathrm{s}}$ is much larger than the precession time $\tau_{\mathrm{ex}}$, $\tau_s \gg \tau_{ex}$, the final term of Eq. (2.8) is negligible and the steady-state component of the non-equilibrium carrier spin polarization is perpendicular to the magnetization $\hat{\mathbf{M}}$ and can be described by $|\delta\mathbf{s}_{\perp}|/\tau_{\mathrm{ex}} = P|\hat{\mathbf{n}} \times \hat{\mathbf{M}}|$. As a result of this polarization, STT acts upon the magnetization as

$$cS\frac{d\hat{\mathbf{M}}}{dt} = P\hat{\mathbf{M}} \times (\hat{\mathbf{n}} \times \hat{\mathbf{M}})\,. \tag{2.9}$$

This this case, the complete spin angular momentum is transferred from the injected polarized carriers to the magnetization (independent of $\tau_{\mathrm{s}}$, $\tau_{\mathrm{ex}}$). The theoretical description of adiabatic STT was developed by [37, 38], which generated a large area research into magnetic tunnel junctions in metals and other electrically controlled magnetization dynamics [29] and ultrafast photo-magnetic laser excitations of ferromagnetic semiconductors. [35, 36]

The second case, in the limit $\tau_s \ll \tau_{ex}$, the $\delta\mathbf{s}$ is parallel to the injected spin polarization $\hat{\mathbf{n}}$ and its magnitude given by $|\delta\mathbf{s}| = P\tau_s$. This is known as the non-adiabatic or field-like STT, [33]

$$cS\frac{d\hat{\mathbf{M}}}{dt} = \frac{\tau_s}{\tau_{ex}}P(\hat{\mathbf{M}} \times \hat{\mathbf{n}})\,, \tag{2.10}$$

and is perpendicular to the adiabatic STT with magnitude $|\delta\mathbf{s}|/\tau_{ex} = P\tau_s/\tau_{ex}$.In the intermediate regime, both adiabatic and non-adiabatic STTs may be present, and the ratio of their magnitudes (non-adiabatic to adiabatic) is defined as $\beta = \tau_{ex}/\tau_s$. [33–35]. An important result of the non-adiabatic STT is the non-zero mobility of a DW in the low-current steady-flow regime. Generally, one can describe the DW mobility as the ratio of $\beta/\alpha$, where $\alpha$ is the damping parameter. [33, 34, 39, 40]

### 2.4.2 Current-induced spin-orbit torque

Unlike the real-space transfer of angular momentum from a spin-polarized current (or polarizer) into a non-collinear ferromagnet in STT, in uniform ferromagnets with inversion asymmetry a momentum-space transfer of angular momentum can occur at the microscopic level even with an unpolarized current. This so-called current-induced SOT, originates from the effective magnetic field generated by the ISGE as predicted by Manchon and Zhang [41] and elaborated in Refs. [22, 42–46].

The current-induced SOT can be thought of in terms of linear-response transport theory, as the redistribution of occupied carrier states on the Fermi surface and deformation of the states by the applied electric field. Following from the description of the ISGE in Sec. 2.2.1, the applied electric field generates a non-equilibrium steady-state spin polarization of the carriers in systems with broken inversion symmetry.

As in the case of STT, when the carrier polarization is misaligned with the local moments, it acts as a torque on the magnetization. [22, 41, 42]

$$cS\frac{d\hat{\mathbf{M}}}{dt} = \frac{1}{\tau_{\rm ex}}(\hat{\mathbf{M}} \times \delta\mathbf{s}_{\rm ISGE})\,. \tag{2.11}$$

Previous demonstrations of this current-induced SOT have been realized in current-asisted magnetization reveal experiments in ferromagnetic semiconductors and metal thin films, [43,44] in spin-orbit driven ferromagnetic resonance measurements, [45,47] and thin-film metal ferromagnets [48]. The DMS ferromagnets (Ga,Mn)As and (Ga,Mn)(As,P) considered here are ideal for experimental studies of both STT [49],and current-induced SOT [23, 42–46].The strong exchange interactions between local Mn moments and carrier spins and strong SOC, combined with the broken inversion symmetry in the strained zinc-blends band structure, provides all of the necessary conditions for generating SOTs in theses materials. As discussed in Sec. 2.2, the symmetry breaking terms can be modified via substrate lattice mismatching (growth) and applied piezostrain (shear). [50]

# 3 MODELING CURRENT-INDUCED SPIN ORBIT TORQUES

## 3.1 Introduction

Utilizing SOTs in novel device designs requires a complete understanding of their microscopic origin as well as potential manipulation techniques. The torques responsible for electrically-driven DW motion in (Ga,Mn)(As,P) occur when the effective field produced by the non-equilibrium spin polarization of the carriers acts on the magnetization. The origin of this current-induced non-equilibrium polarization is twofold: the extrinsic $\delta\mathbf{s}^{ext}$ contribution from the non-equilibrium steady-state redistribution of the carriers [42, 43], and the intrinsic $\delta\mathbf{s}^{int}$ component generated by the polarization of the carriers themselves [21]. The SOT is then modeled as the interaction between the uniform magnetization and the effective magnetic field. The model discussed in this thesis calculates both contributions and assesses their dependence on a wide range of experimental parameters.

## 3.2 Theoretical Method

### 3.2.1 Origin

SOTs arise from the interaction between the local magnetization in a system and the collective spin polarization of its carriers. In uniform dilute ferromagnetic semiconductors with broken inversion symmetry and strong SOC, such as (Ga,Mn)As and (Ga,Mn)(As,P), an applied electric field results in steady-state non-equilibrium carrier spin polarization via the ISGE. This polarization can be modeled as an effective current-induced field $\delta\mathbf{H}$. In Mn-doped GaAs compounds, the non-equilibrium carrier spin polarization originates from the interaction between localized Mn magnetic moments (d-orbitals) and delocalized carriers (holes) yielding both extrinsic and intrinsic contributions. The ISGE, which depends on the crystalline strain and the applied electric field, but is relatively unaffected by the magnetization- produces

the extrinsic term. This is associated with the non-adiabatic (field-like) SOTs. The symmetry of the field can be controlled by strain-mediated turning of the SOC interaction, and includes both Rashba and Dresselhaus terms. The intrinsic component of the non-equilibrium carrier spin-polarization can be attributed to the polarization of the carriers between scattering events. This depends solely on the band structure of the material system, and comes from the so-called inter-band terms. The intrinsic contribution accounts for the out-of plane current-induced spin polarization, and results in non-adiabatic (anti-damping) SOTs.

As discussed in the previous sections, the phenomenology of current-induced SOT is simplified in dilute moment ferromagnetic semiconductors, in which the magnetization dynamics (slow) and carrier spin dynamics (fast) can be decoupled.In such systems, the carriers can be modeled using a Hamiltonian with a kinetic exchange coupling term

$$H = H_0 + H_{\text{ex}}, \qquad H_{\text{ex}} = J_{\text{ex}} cS\hat{\mathbf{M}} \cdot \boldsymbol{\sigma}. \tag{3.1}$$

Here $H_0$ is the Hamiltonian for the current-carrying states and can be replaced by the Kohn-Luttinger Hamiltonian for hole systems, or a Rashba Hamiltonian for two-dimensional electron gas. The exchanged coupling is given by $J_{\text{ex}}$, the vector of carrier spin matrices follows $\boldsymbol{\sigma} \equiv (\sigma_x, \sigma_y, \sigma_z)$, with Pauli matrices ( $4 \times 4$ Luttinger spin matrices) as components for systems with electrons (holes) as carriers.

Beginning with the equilibrium condition, the carrier spin density is aligned with the magnetization. The non-equilibrium spin polarization arising from the ISGE is misaligned with the orientation of the local magnetic moments. Thus, the current-induced SOT acts upon the magnetization as described by Eq. 2.11. Phenomenologically, this can be described as the precession of the magnetization in an effective magnetic (current-induced field). $\delta\mathbf{H}$. The magnetization dynamics in the effective field are well modeled using the Landau-Lifshits-Gilbert equation

$$\frac{d\hat{\mathbf{M}}}{dt} = -\gamma\hat{\mathbf{M}} \times (\mathbf{H} + \delta\mathbf{H}) + \alpha\frac{d\hat{\mathbf{M}}}{dt} \times \hat{\mathbf{M}} \tag{3.2}$$

where $\mathbf{H}$ is the external magnetic field, $\alpha$ is the Gilbert damping constant and $\gamma = ge/2m_0$ is the gyromagnetic factor with $e$ elementary charge, $m_0$ electron mass. Comparing Eq. (3.2) to Eq. (2.11) we obtain

$$\delta\mathbf{H} = -\frac{J_{\mathrm{ex}}}{g\mu_{\mathrm{B}}}\delta\mathbf{s}, \tag{3.3}$$

where $\mu_{\mathrm{B}}$ is the Bohr magneton. It is important to note that the coupling constant is $J_{\mathrm{ex}}$, as seen in Eq. (3.1), not the carrier $g$-factor found in [43]. The $g$-factor in Eq. (3.3) corresponds to the localized electrons and is $g = 2$ in the case of Mn $d$-electrons in (Ga,Mn)As.

### 3.2.2 Intraband and interband contributions

The intraband component of the steady-state non-equilibrium spin polarization arises from the redistribution of carriers on the Fermi surface. The perturbation of the carrier states (also a result of the ) corresponds to the inter band term of the current-induce spin-orbit field. [18–20]

$$\delta\mathbf{s} = \delta\mathbf{s}^{\mathrm{intra}} + \delta\mathbf{s}^{\mathrm{inter}} = \frac{1}{V}\sum_{\mathbf{k},a}\langle\boldsymbol{\sigma}\rangle\delta f + \frac{1}{V}\sum_{\mathbf{k},a}\langle\delta\boldsymbol{\sigma}\rangle f. \tag{3.4}$$

Here, momentum $\mathbf{k}$ and band index $a$ are used to identify the carrier states, $f$ is the nonequilibrium steady state carrier distribution function, and the change from the equilibrium Fermi-Dirac distribution $f_0$ is defined as $\delta f = f - f_0$. There are two approaches to calculating these components. The semiclassical Boltazman formalism can be used to derive the intraband terms directly, [42] while Kubo linear formalism for time-dependent perturbation theory can be used to calculate both intraband and interband terms.

### 3.2.3 Semiclassical and Kubo formalisms

Taking the relaxation time approximation of the Boltzman equation for $\delta\mathbf{s}^{\text{intra}}$ in Eq. (3.3) we find the semiclassical expression for the intraband

$$\delta\mathbf{H}^{\text{intra}} = -\frac{J_{\text{ex}}}{g\mu_B V}\sum_{\mathbf{k},a}\frac{\hbar}{2\Gamma}\left(\boldsymbol{\sigma}\right)_a\left(e\mathbf{E}\cdot\mathbf{v}\right)_a\delta(E_{\mathbf{k}a}-E_F). \tag{3.5}$$

The Fermi energy is $E_F$, and electronic states $|\mathbf{k}a\rangle$. The Fermi-Dirac distribution functions $f_{\mathbf{k}a}$ correspond to band energies $E_{\mathbf{k}a}$, and the spectral broadening is given by $\Gamma = \hbar/2\tau$ where $\tau$ is the relaxation time. The velocity operator for the carriers is $\mathbf{v}$ and $\mathbf{E}$ is the external electric field. In this notation, matrix elements of an operator $\hat{C}$ are given by $(\hat{C})_{ab} \equiv \langle\mathbf{k}a|\,\hat{C}\,|\mathbf{k}b\rangle$ or $(\hat{C})_a \equiv \langle\mathbf{k}a|\,\hat{C}\,|\mathbf{k}a\rangle$. The interband term can be written of integrals over the Fermi surface and Fermi sea in the low disorder limit

$$\begin{aligned}
\delta\mathbf{H}^{\text{inter}} &= \delta\mathbf{H}^{(1)} + \delta\mathbf{H}^{(2)} \\
\delta\mathbf{H}^{(1)} &= \frac{\hbar J_{\text{ex}}}{g\mu_{\text{B}}V}\sum_{\mathbf{k},a\neq b}2[(\boldsymbol{\sigma})_{ab}(e\mathbf{E}\cdot\mathbf{v})_{ba}] \\
&\times \frac{\Gamma(E_{\mathbf{k}a}-E_{\mathbf{k}b})}{[(E_{\mathbf{k}a}-E_{\mathbf{k}b})^2+\Gamma^2]^2}(f_{\mathbf{k}a}-f_{\mathbf{k}b}) \\
\delta\mathbf{H}^{(2)} &= \frac{\hbar J_{\text{ex}}}{g\mu_{\text{B}}V}\sum_{\mathbf{k},a\neq b}2[(\boldsymbol{\sigma})_{ab}(e\mathbf{E}\cdot\mathbf{v})_{ba}] \\
&\times \frac{\Gamma^2-(E_{\mathbf{k}a}-E_{\mathbf{k}b})^2}{[(E_{\mathbf{k}a}-E_{\mathbf{k}b})^2+\Gamma^2]^2}f_{\mathbf{k}a}.
\end{aligned} \tag{3.6}$$

From the linear response, one can find the non-equilibrium spin densities $\delta\mathbf{s}$. Using the Green's functions, following [23], Eqs. (3.5) and (3.6) can be rewritten as $G^R_{\mathbf{k}a}(E)|_{E=E_F} \equiv G^R_{\mathbf{k}a} = 1/(E_F - E_{\mathbf{k}a} + i\Gamma)$, with $G^A = (G^R)^*$ giving the Kubo formula

$$\delta\mathbf{H} = -\frac{\hbar J_{\text{ex}}}{2\pi g\mu_{\text{B}}V}\sum_{\mathbf{k},a,b}(\boldsymbol{\sigma})_{ab}(e\mathbf{E}\cdot\mathbf{v})_{ba}[G^A_{\mathbf{k}a}G^R_{\mathbf{k}b} - G^R_{\mathbf{k}a}G^R_{\mathbf{k}b}]. \tag{3.7}$$

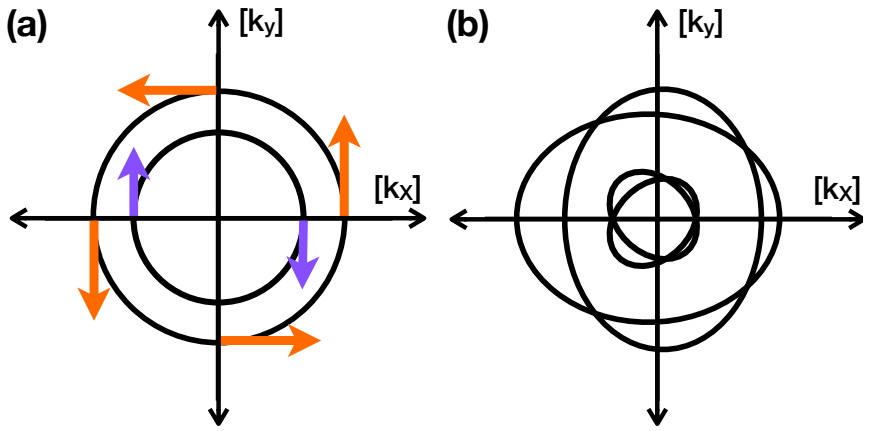


**Fig. 3.1.** Fermi surfaces for space inversion asymmetric systems: **(a)** 2DEG with Rashba-type SOI coupling proportional to $(k_x\sigma_y - k_y\sigma_x)$. Arrows denote the spin expectation values for the two sub-bands. **(b)** Four-band Luttinger model within spherical approximation, including strain-induced SOC (symmetry breaking).

### 3.2.4 Symmetry breaking

As discussed in Sec. 2.2.2, the presence of a symmetry breaking term is a prerequisite for the ISGE to occur. In inversion symmetric systems, the current-induced spin-orbit field (SOF) will cancel, as seen in Eqs. (3.5,3.6,3.7). [23] For space-inversion symmetric Hamiltonians, the eigenstates $|\mathbf{k}a\rangle$ and $|-\mathbf{k}a\rangle$ differ by a phase factor, so the component of the spin along $\alpha$ (an arbitrary orientation) obeys $(\sigma_\alpha)_{\mathbf{k}a} = (\sigma_\alpha)_{-\mathbf{k}a}$. The corresponding eigenenergies are $E_{\mathbf{k}a} = E_{-\mathbf{k}a}$, and one expects the group velocities $\mathbf{v}_{\mathbf{k}a} = \frac{1}{\hbar}\frac{\partial E_{\mathbf{k}a}}{\partial \mathbf{k}}$ to change sign under space inversion, $\mathbf{v}_{\mathbf{k}a} = -\mathbf{v}_{-\mathbf{k}a}$. This is equivalent to noting the expressions in Eqs. (3.5,3.6,3.7) are odd in momentum, and the intraband SOF will cancel if the Fermi surface is space inversion-symmetric. In the case of the interband contribution, the cancellation for inversion symmetric systems is shown by $\langle -\mathbf{k}a|\,\boldsymbol{\sigma}\,|-\mathbf{k}b\rangle\,\langle -\mathbf{k}b|\,\partial\hat{H}/\partial(-\mathbf{k})\,|-\mathbf{k}a\rangle = -\langle \mathbf{k}a|\,\boldsymbol{\sigma}\,|\mathbf{k}b\rangle\,\langle \mathbf{k}b|\,\partial\hat{H}/\partial\mathbf{k}\,|\mathbf{k}a\rangle$ where $\hat{H}(\mathbf{k}) = \hat{H}(-\mathbf{k})$. Following this argument, one can conclude that there will be

no current-induced SOF in any space-inversion symmetric systems. It is important to note that this restriction includes magnetic systems with broken time-reversal symmetry.

The effect of the inversion symmetry breaking is shown in Fig.3.1a for a 2DEG with Rashba SOC and Fig.3.1b for a hole gas described by the 4-band Luttinger model. In the case of the hole gas (Fig. 3.1b), the Fermi surface inversion asymmetry is a direct result of the non-zero growth strain. For $\epsilon_{ii} = \epsilon_{ij} = 0$, the current-induced SOF would be zero. [23,43] For the 2DEG with Rashba SOC, the inversion symmetry breaking occurs in the Hamiltonian, and the Fermi surface remains inversion symmetric. This can be seen in the asymmetry of the eigenfunctions, and again in the spin expectation values (arrows in Fig. 3.1a), producing a non-zero current-induced SOF [41, 42] if electrons couple with the magnetization.

### 3.2.5 Model

The system is described in the hole picture by the four-band Kohn-Luttinger Hamiltonian, with exchange interaction and strain (growth and applied) modeled for ferromagnetic semiconductors. The Hamiltonian for the system is

$$H = H_{\mathrm{KL}} + H_{\mathrm{exch}} + H_{\mathrm{strain}}. \tag{3.8}$$

The initial term is the four-band Kohn-Luttinger Hamiltonian,

$$H_{\mathrm{KL}} = \frac{\hbar^2 k^2}{2m_0}\left(\gamma_1 + \frac{5}{2}\gamma 2\right)\mathbf{I}_4 - \frac{\hbar^2}{m_0}\gamma_3\left(\mathbf{k}\cdot\mathbf{J}\right)^2 + \frac{\hbar^2}{m_0}(\gamma_3 - \gamma_2)\left(k_x^2 J_x^2 + k_y^2 J_y^2 + k_z^2 J_z^2\right), \tag{3.9}$$

which is written in terms of the hole momentum, $\mathbf{k}$, Luttinger parameters, $\gamma_{1,2,3}$, and angular momentum matrices of the carrier holes, $\mathbf{J} = (J_x, J_y, J_z)$. The electron mass

is $m_0$, and $\mathbf{I}_4$ is the $4 \times 4$ identity matrix. The second term describes the exchange interaction between the localized Mn moments and itinerant carriers (holes),

$$H_{\text{exch}} = J_{\text{pd}} S_{\text{Mn}} c_{\text{Mn}} \hat{\mathbf{M}} \cdot \boldsymbol{\sigma}. \tag{3.10}$$

The strength of the exchange coupling between the Mn $d$-orbitals and $p$-state carriers is given by $J_{\text{pd}}$, $S_{\text{Mn}} = 5/2$ is the Mn spin, $c_{\text{Mn}}$ is concentration of Mn dopant ions, $\hat{\mathbf{M}}$ is the magnetization vector, and $\boldsymbol{\sigma}$ are the spin matrices for holes, such that $J = 3\boldsymbol{\sigma}$ [51]. The final term includes the strain,

$$\begin{aligned} H_{\text{strain}} &= -b\left[\left(J_x^2 - \frac{\mathbf{J}^2}{3}\right)\epsilon_{xx} + \text{c.p.}\right] \\ &\quad + C_4\left[J_x\left(\epsilon_{yy} - \epsilon_{zz}\right)k_x + \text{c.p.}\right] \qquad (3.11) \\ &\quad + C_5\left[\epsilon_{xy}(k_y J_x - k_x J_y) + \text{c.p.}\right]. \qquad (3.12) \end{aligned}$$

where $\epsilon_{ij}$ is the strain tensor and $b$ is the axial deformation potential. The coefficients $C_4$ and $C_5$ are the magnitude of the momentum-dependent Dresselhaus-symmetric and Rashba-symmetric strain terms respectively. We use the value $C_4 = 5\text{eV}\text{Å}$ calculated [52] from first principles for holes in (Ga,Mn)As and $C_5 = C_4$. [1] Notation: for pure growth strain ($\epsilon_{xy} = 0$) we take $\epsilon_{xx} = \epsilon_{yy} = 0$, $\epsilon_{zz} = \epsilon_0$. The first term of the strain Hamiltonian is momentum independent, and thus not sufficient for the generation of SOF, while the subsequent momentum-dependent terms are critical because they result in broken space inversion symmetry. [22, 43]

In the Sec. 3.3 we summarize the results of calculations for a broad range of experimentally relevant parameters including Dresselhaus (growth) and Rashba (shear) strain, crystal orientation, Mn concentration, and compensation. Of primary interest for spintronics applications and the experiments discussed in Sec. 4 is the relationship between the orientation of the local magnetic moment and the resulting

[1] To date, there have been no measurements or calculations of $C_5$ in (Ga,Mn)As

current-induced SOF, which is the focus of this discussion. Unless otherwise stated, the applied electric field is $E = 0.1\text{mV/nm}$ and the disorder broadening is set to $\Gamma = \hbar/2\tau = 50\text{meV}$.

## 3.3 Results

In this section, the current-induced SOFs are calculated under a range of experimentally relevant conditions. For each parameter evaluated, we show both the intraband and interband contributions, as well as the total field. The dependence of the induced SOF on magnetization orientation is discussed in Sec. 3.3.1. Sec. 3.3.2 focuses on the current direction versus crystal axis orientation. The the dependence oh the symmetry and strength of the strain are found in Sec. 3.3.3. These results represent a fraction of the parameter space which was investigated during the project. A table of additional parameters which have been calculated, but are not discussed in this thesis is located in Appendix C

### 3.3.1 Magnetization orientation

When evaluating current-induced SOT as a mechanism for manipulating the orientation of local moments in uniform ferromagnetic semiconductors, particularly current-induced DW motion application, the main concern is the behavior of the field generated in regions of inhomogeneous magnetization. We are interested in both uniformity of the orientation of the SOF as well as any variations in the field strength for different magnetization orientations. Theses characteristics are key to determining how current-induced SOTs will effect the structure of DWs and other regions of inhomogenous magnetization. In order for this to be a viable option for magnetization manipulation, the structure of the DW must be preserved as it is moved.

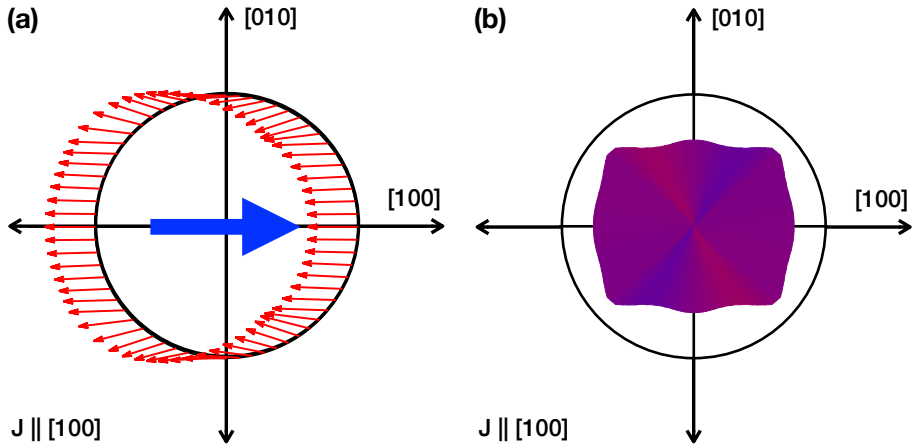


**Fig. 3.2.** Current-induced SOF for (Ga,Mn)As with Dresselhaus-type growth strain ($\epsilon_{xx} \neq 0$) oriented along the [100] crystal axis. Radius is 0.50 mT. **(a)** Arrows denote the field strength and orientation as a function of the angle of local magnetization versus [100] crystal axis for the total effective field. **(b)** SOF strength (magnitude of the radial vector) with respect to the magnetization orientation. Colour depicts deviation from average direction

Our results show that while there is some variation in the strength of the field generated for different magnetization directions, there are only small deviations from the average direction. The primary contribution comes from the magnetization-independent ISGE, the orientation of which follows the strain symmetry as discussed in Sec. 3.3.3. In Fig. 3.2a, we see the current-induced SOF for a current applied along the [100] crystal axis of (Ga,Mn)As for a system with carrier (hole) density $p = 1.0$ V/nm$^3$ and Mn content $x = 4\%$. The arrows in Fig. 3.2a show CIF $\delta H_{100}$ as a function of in-plane magnetization orientation $\hat{M} = (-\sin\phi, \cos\phi, 0)$, $0 \leq \phi \leq 2\pi$.

The dominant field is oriented antiparallel to the applied current. In Fig. 3.2b, the strength of the field is plotted as magnitude of the radial vector with respect to the magnetization orientation. The colour shows the variation in the orientation

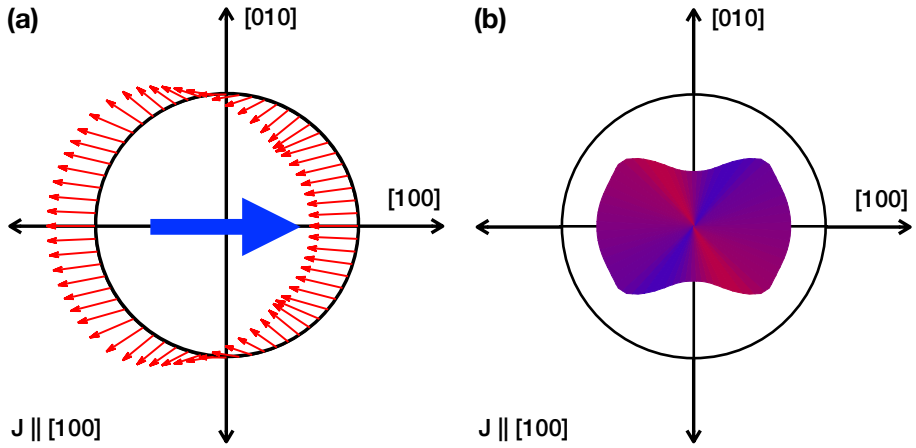


**Fig. 3.3.** Intraband component of current-induced SOF for (Ga,Mn)As with Dresselhaus-type growth strain ($\epsilon_{xx} \neq 0$) oriented along the [100] crystal axis. **(a)** Arrows denote the field strength and orientation as a function of the angle of local magnetization versus [100] crystal axis. **(b)** SOF strength (magnitude of the radial vector) with respect to the magnetization orientation. Colour depicts deviation from average direction.

of the SOF, with purple corresponding to the average direction of the field and red (blue) corresponding to $\pm\pi/2$ radians from average.

The intraband component, Fig. 3.3, provides the main contribution to the total field antiparallel to the applied current, however there are significant variations in the strength and orientation of the field as a function of magnetization angle. The interband component, Fig. 3.4, is significantly weaker than the intraband, with the orientation and strength very strongly dependent on the magnetization angle. The total SOF, however, shows a significant reduction in the angular dependence.

### 3.3.2 Current direction

The effect of the crystal orientation (the direction of applied current) is determined by the uniaxial anisotropy in strained (Ga,Mn)As ((Ga,Mn)(As,P)). In Fig. 3.5

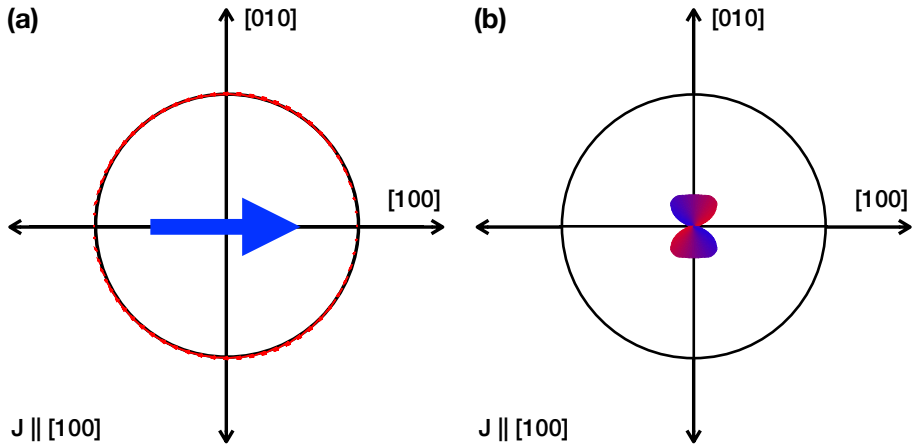


**Fig. 3.4.** Interband component of current-induced SOF for (Ga,Mn)As with Dresselhaus-type growth strain ($\epsilon_{xx} \neq 0$) oriented along the [100] crystal axis. **(a)** Arrows denote the field strength and orientation as a function of the angle of local magnetization versus [100] crystal axis. **(b)** SOF strength (magnitude of the radial vector) with respect to the magnetization orientation. Colour depicts deviation from average direction.

we show that the effective field is strongly dependent upon the direction of applied current relative to the crystal orientation, as confirmed by previous experimental results. [21, 43, 45, 53] It important to note in comparison with experiments that the angle $\phi$ refers to the magnetization orientation with respect to the [100] crystal axis, while the angle $\theta$ refers the the relative orientation of the magnetization to the direction of current.

The field $\langle \delta H_{100} \rangle$ is parallel to the electric current and $\langle \delta H_{010} \rangle$ is antiparallel. SOFs for arbitrary directions of the electric field can be obtained as a linear combination of $\langle \delta H_{100} \rangle$ and $\langle \delta H_{010} \rangle$ since the effective field is linearly dependent on the electric field as one can see from Eq. (3.5). The dependence of the average over all magnetization angles SOFs direction as a function of electric field orientation follows the the central panel, Fig. 3.6b, and is consistent with the Dresselhaus-type symmetry found in the experiments. [43, 45]

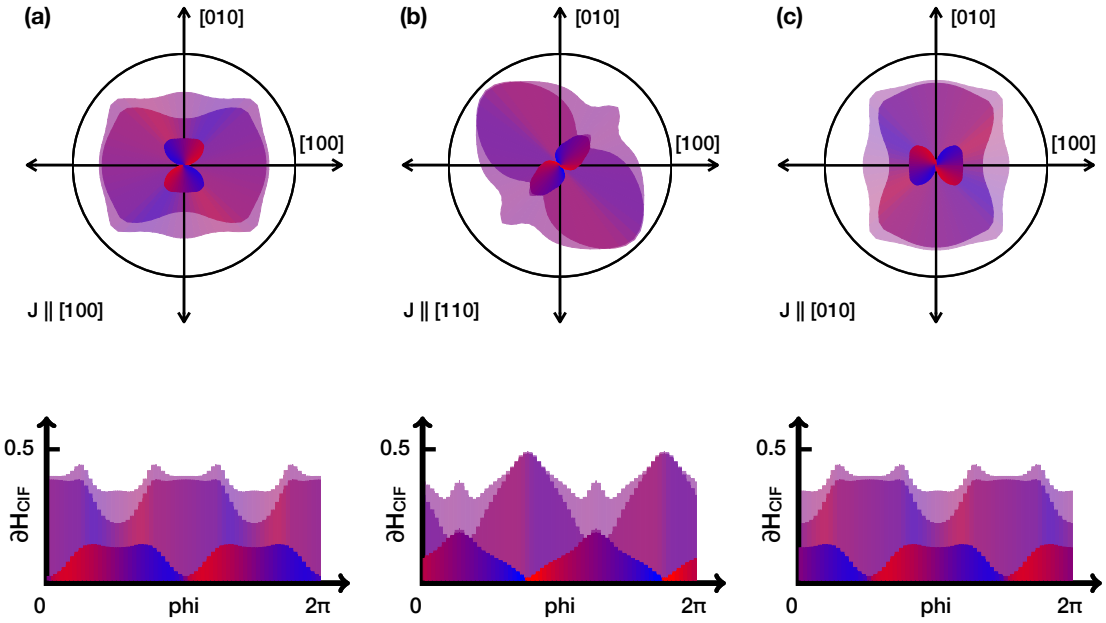


**Fig. 3.5.** Current-induced SOF for (Ga,Mn)As with Dresselhaus-type growth strain ($\epsilon_{xx} \neq 0$) oriented along the [100], [110], and [010] crystal axes. Each diagram includes the intraband and interband components overlaid on the combined effective field. SOF strength as magnitude of the radial vector with respect to the magnetization orientation (Radius = 0.5 mT). The colour depicts deviation from average direction. Opacity is used to distinguish between components (least opaque to most opaque: combined, intraband, interband). **Top:** Figures show the field generated as a radial plot of different magnetization orientations for current applied along **(a)** [100], **(b)** [110], and **(c)** [010] crystal axes. **Bottom:** Data plotted with the x axis corresponding to different angles of magnetization relative to the [100] crystal axis.

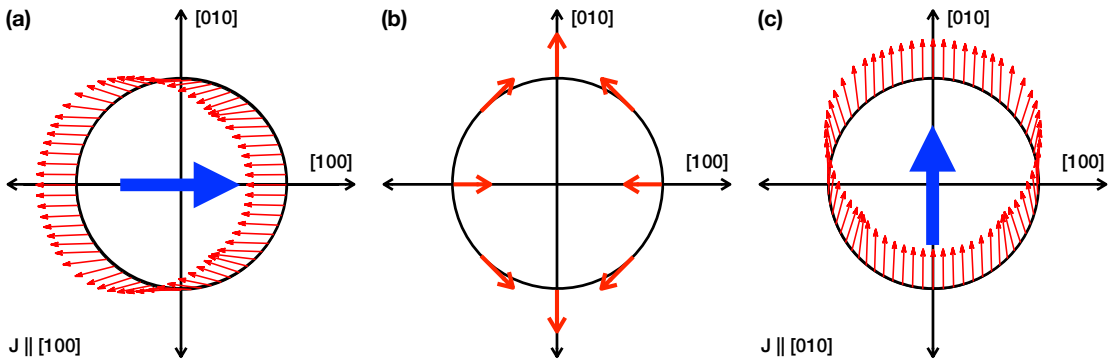


**Fig. 3.6.** Average direction and strength of current-induced SOF for (Ga,Mn)As with Dresselhaus-type growth strain ($\epsilon_{xx} \neq 0$), as a function of current direction. **(a)** Arrows denote the total effective field strength and orientation as a function of the angle of local magnetization versus [100] crystal axis for current applied along [100]. **(b)** Angle-averaged SOF generated by currents along various crystalline axes. **(c)** Arrows denote the field strength and orientation as a function of the angle of local magnetization versus [100] crystal axis for current along [010].

### 3.3.3 Strain

As discussed in Sec. 2.2.1, in (Ga,Mn)As and other zinc-blends semiconductors, the inversion symmetry breaking necessary to generate the effective magnetic field is a direct result of the strain, and will follow the corresponding symmetry. For growth strained (Ga,Mn)As of $-0.03\%$ (Dresselhaus), we see the expected symmetry for different directions of applied electric field (current) in Fig. 3.6. For applied shear strain (Rashba) of $-0.03\%$ we see a much weaker effective magnetic field (approximately $1/5^t h$ of the corresponding Dresselhaus field). The expected Rashba symmetry is confirmed by our simulations, Fig. 3.7, and we note that once again the effective field generated for different crystal orientations can be written as a linear combinations of the fields generated along [100] and [010]. Comparing the results of the intraband, interband, and total current-induced SOFs for shear strain (Fig. 3.8) with

the results for growth strain (Fig. 3.5), we note that the generated field components differ significantly.

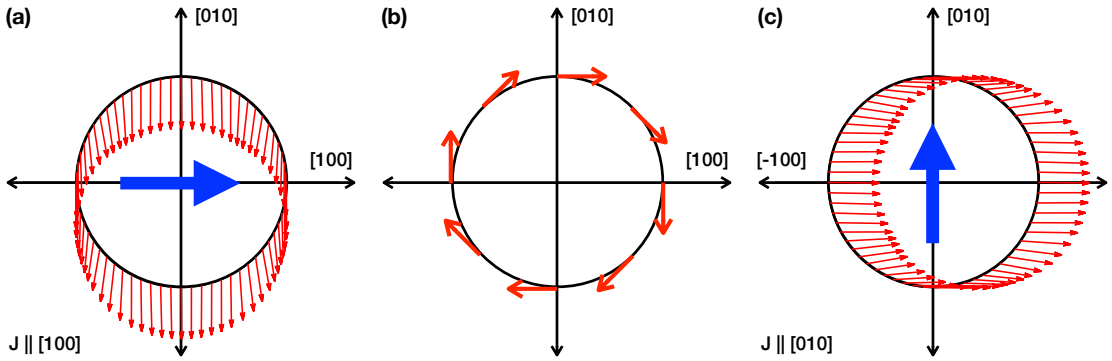


**Fig. 3.7.** Average direction and strength of current-induced spin-orbit field (SOF) for (Ga,Mn)As with Rashba-type growth strain ($\epsilon_{xy} \neq 0$), as a function of current direction. **(a)** Arrows denote the total effective field strength and orientation as a function of the angle of local magnetization versus [100] crystal axis for current applied along [100]. **(b)** Angle-averaged SOF generated by currents along various crystalline axes. **(c)** Arrows denote the field strength and orientation as a function of the angle of local magnetization versus [100] crystal axis for current along [010].

In the case of growth (Dresselhaus) strain, the intraband component is dominant for all relative angles of magnetization in the [100] and [010] microbars, however for the diagonal [110] or [1$\bar{1}$0] bars the interband contribution is equivalent to or close to equivalent to the intraband contribution when the magnetization is aligned nearly parallel (antiparallel) to the current direction. For comparison with experiments, we estimate that the effective sheer strain induced would be an order of magnitude smaller than the growth strain. Here we used the same magnitude for both growth and applied strain (-0.03%) in order to demonstrate the difference in the magnitude of the resulting current-induced SOFs.

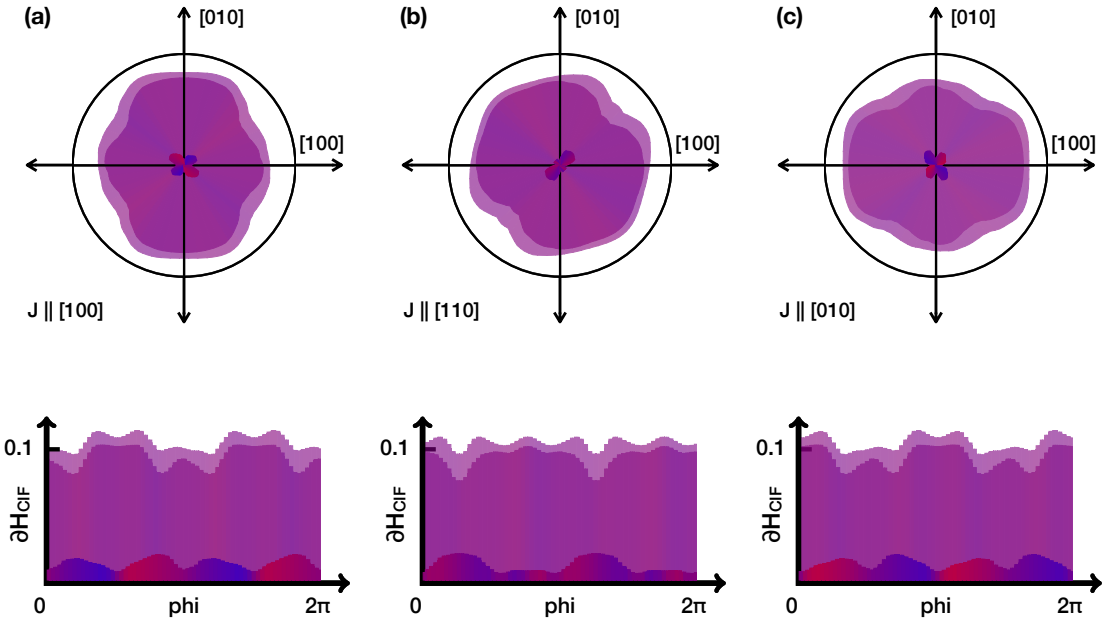


**Fig. 3.8.** Current-induced SOF for (Ga,Mn)As with Rashba-type growth strain ($\epsilon_{xy} \neq 0$) oriented along the [100], [110], and [010] crystal axes. Each diagram includes the intraband and interband components overlaid on the combined effective field. SOF strength as magnitude of the radial vector with respect to the magnetization orientation (Radius = 0.125 mT). The colour depicts deviation from average direction. Opacity is used to distinguish between components (least opaque to most opaque: combined, intraband, interband). **Top:** Figures show the field generated as a radial plot of different magnetization orientations for current applied along **(a)** [100], **(b)** [110], and **(c)** [010] crystal axes. **Bottom:** Data plotted with the x axis corresponding to different angles of magnetization relative to the [100] crystal axis.

# 4 CURRENT-INDUCED DOMAIN WALL MOTION IN (GA,MN)(AS,P) MICROBARS*

## 4.1 Introduction

The fully-electric control of DW motion has been a much sought after goal in the design of novel electronics. DW mobility is typically separated into two regimes; steady and precession motion, with different mobilities. Below the so-called Walker breakdown (WB) the DW velocity vs. current density curve is linear, above the WB critical current density there is a sharp cusp and a region of non-linear precessional motion. By manipulating the magnetic anisotropy of (Ga,Mn)(As,P) using piezoelectric strain, these experiments investigate its potential to shift the WB, establishing strain-modified DW mobility as a tool for electrically controlled DW motion.

## 4.2 Fabrication

Novel experiments utilizing polarized spin currents (spin transfer torque STT) to manipulate magnetic domains have shown important characteristics for the development of the non-volatile down-scalable logic and memory elements for such devices. [29, 54–61] While these techniques have been previously demonstrated in layers structures [37,38,62–64], and magnetic insulators [65,66], the dilute ferromagnetic semiconductors discussed here provide superior environment to study STT as it pertains to DW motion. [67–69] The materials used for these experiments, e.g. the (III,V) semiconductor (Ga,Mn)As, are plagued by several experimental difficulties, such as domain wall pinning sites (material and/or pattern defects which prevent DWs from traveling) and measurement issues, due to sample quality.

*Reprinted with permission from "Piezoelectric control of the mobility of a domain wall driven by adiabatic and non-adiabatic torques" by E. De Ranieri, P. E. Roy, D. Fang, E. K. Vehstedt, A. C. Irvine, D. Heiss, A. Casiraghi, R. P. Campion, B. L. Gallagher, T. Jungwirth, and J. Wunderlich, "Piezoelectric control of the mobility of a domain wall driven by adiabatic and non-adiabatic torques", Nat. Mater., 12, 808 – 814 Copyright 2013 by Nature Publishing Group.

This study focuses on STT-driven DW motion in phosphorus doped (Ga,Mn)As, ((Ga,Mn)(As,P)), which has several advantages over traditional (Ga,Mn)As, discussed in Sec. 2.1.2. As in the case of the ubiquitous (Ga,Mn)As, (Ga,Mn)(As,P) exhibits both strong SOC and exchange interaction; carrier transport in (Ga,Mn)(As,P) occurs via the As valence band holes (p-orbital), magnetization results from Mn local moments (d-orbital), and the exchange coupling between the hole-carriers and local moments is mediated by p-d hybridization. An important characteristic for this experiment is the relative strength of the $\tau_s \sim \tau_{ex}$ due to the strong SO and exchange interactions, this provedes an ideal environment to investigate the behavior of adiabatic and non-adiabatic STT. [23, 70–72]

By utilizing DMS materials with strong SOC, rather than traditional ferromagnetic metals with higher local moment densities, we gain an additional method of control by employing applied sheer strain to manipulate the magneto-crystalline anisotropy. This is possible because the magneto-crystalline anisotropy fields are much stronger than the demagnetization anisotropy fields in these systems with low saturation moments and strong SOC. [69] The reduced moment density also corresponds to a lower threshold current needed to excite STT-driven magnetization dynamics in DMS. [67, 69, 73] In this work, applied strain is used to modify the magneto-crystalline anisotropy fields so as to stabilize/destabilize a particular DW structure (e.g. Bloch, Néel). This techniques enables precise control over the stability and internal structure of DWs for various sample orientations. The effect of which can be directly observed via shifts in the WB, in good agreement with theoretical predictions. [39, 40, 74]

### 4.2.1 Material

The samples used in the current-induced DW motion experiments are fabricated using 25 nm - thick $(Ga_{1-x},Mn_x)(As_{1-y},P_y)$ grown on GaAs substrates. The wafers are provided by the Spintronics and Ferromagnetic Semiconductor group at the Univer-

sity of Nottingham[1], and are grown by LT - MBE. The manganese and phosphorus concentrations have been optimized to 6% and 10% respectively in previous experiments. [75] The wafers are cut into 5 mm × 5 mm chips along the [110]/[1$\bar{1}$0] crystalline axes, which are then annealed for 48 h at 180 °C. This post-growth annealing has been found to strongly affect the material parameters of both (Ga,Mn)As and (Ga,Mn)(As,P), reducing interstitial defects, increasing the Curie temperature, and shifting the anisotropy from in-plane to perpendicular-to-plane (for P > 9% doping). [76]. The annealed material has a Curie temperature of 115K and conductivity of $230/\Omega/cm$. [77]

### 4.2.2 Devices

Four device samples are patterned on each chip. The devices are comprised of two perpendicular 4 μm × 60 μm bars connected to a 100 μm × 100 μm region. (Fig. 4.1) The unpatterned area is used to study magnetic field driven DW motion. A third bar of the same dimensions, with four contact points, is included in each device and is used to measure resistivity. The devices are prepared in two orientations, with microbars along either [110]/[1$\bar{1}$0] (Fig. 4.2) or [100]/[010] (Fig. 4.3).

### 4.2.3 Patterning

After annealing, the chip is spun with 300 nm - thick PMMA and the sample patterns are written using electron beam (e-beam) lithography. The unused regions of (Ga,Mn)(As,P) are then removed using either reactive ion etching (RIE) leaving the devices electrically isolated. Additional samples were prepared using ion milling rather than RIE to achieve cleaner edges on the microbars. (Fig. 4.4)

A 180 nm - thick layer of PMMA is then spun on the patterned chip and a 6 μm line is cross-linked at the end of each microbar using high-dose e-beam irradiation.

[1]R.P. Campion, B.L. Gallagher, et al.

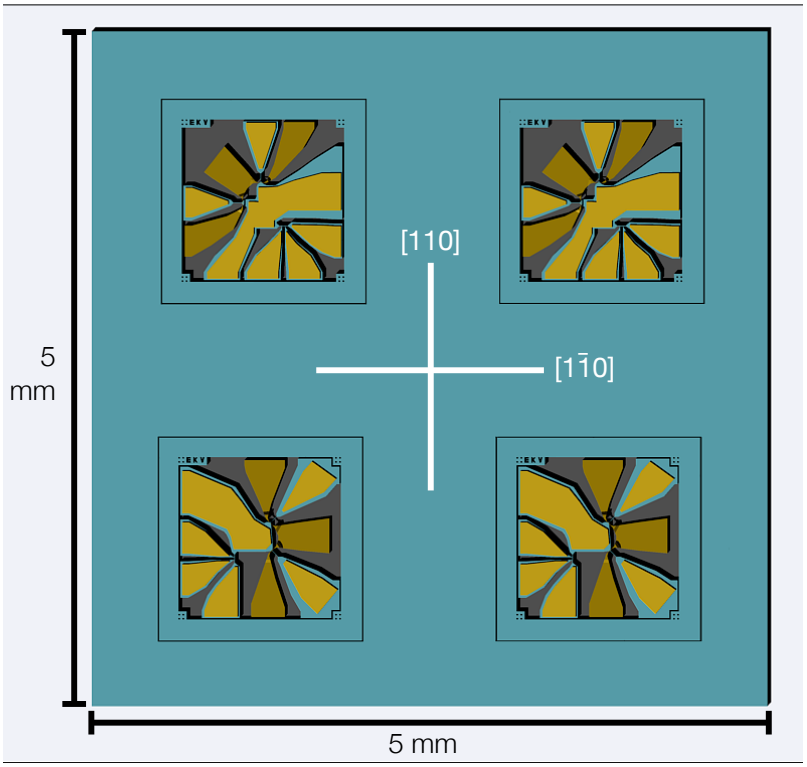


**Fig. 4.1.** Layout of a 5 mm by 5 mm chip with four samples, two with microbars oriented along [100]/[010] and two oriented along [110]/[1$\bar{1}$0].

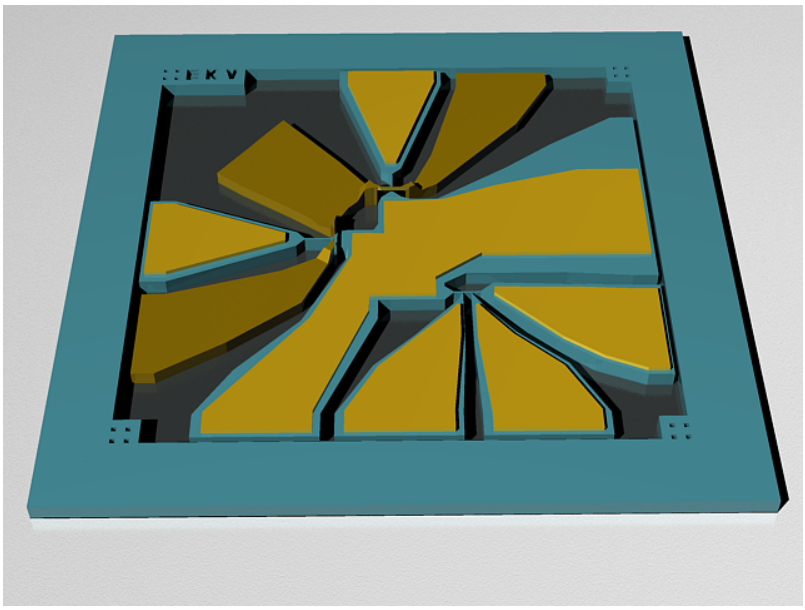

**Fig. 4.2.** Layout of [110]/[1$\bar{1}$0] samples.

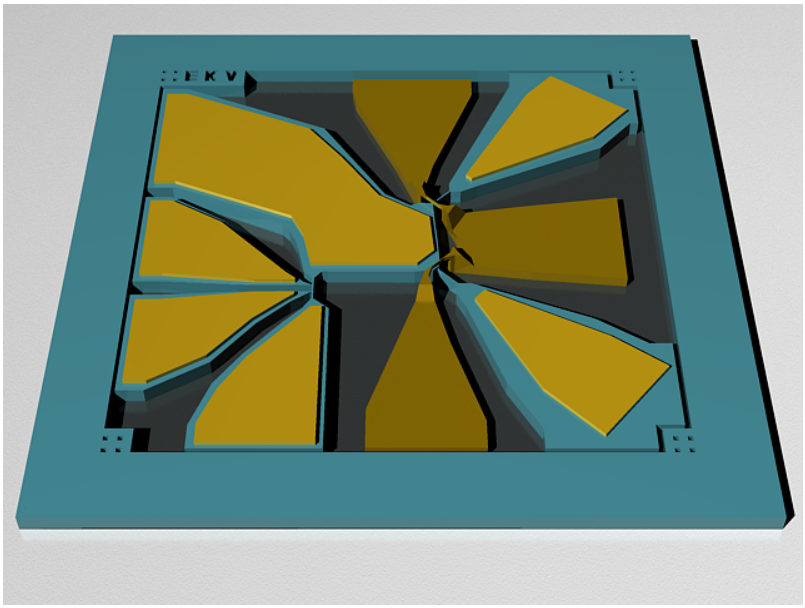

**Fig. 4.3.** Layout of [100]/[010] samples.

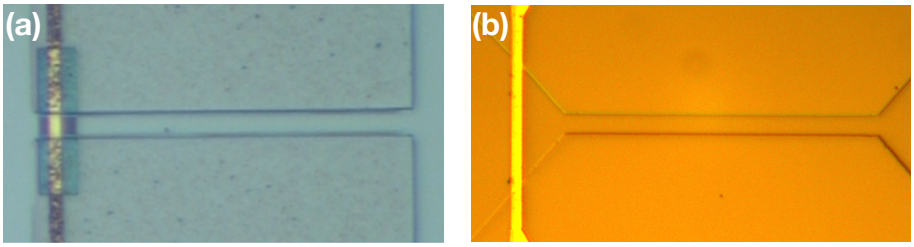


**Fig. 4.4.** Images of samples processed with **(a)** RIE and **(b)** ion milling

These cross-linked regions serve as the support for the Cr/Au strip-line, which is deposited along with the contacts in a subsequent round of e-beam lithography and Cr/Au (20 nm/280 nm) thermal evaporation. The cross-linked PMMA is then removed via oxygen plasma etching, leaving the strip-line bridge separate from the microbars. (See Fig. 4.5) Thus, the CrAu bridge does not induce strain in the microbar, preventing any unintentional DW pinning sites. Detailed instructions and fabrication parameters are included in Appendix B.

### 4.2.4 Packaging

The samples are prepared for piezoelectric measurements following the procedures developed in reference [78]. The chips are thinned to 200 μm, scored, and separated into 4 individual 2.5 m × 2.5 m samples. Each sample is attached to a commercial uniaxial piezo-electric actuator (Piezomechanik GmbH) using a two-component epoxy adhesive (Vishay M-Bond 600), with either the $[1\bar{1}0]$ or [100] microbar oriented along the direction of actuator expansion. Thus a positive (negative) applied voltage, $U$, results in an additional uniaxial tensile (compressive) strain along the $[1\bar{1}0]$ axis, which in turn weakens (strengthens) the $U = 0$ in-plane magnetization easy axis $[1\bar{1}0]$. [50, 79] The sample/stressor combination is then cured following one of two procedures: pre-biased samples are cured under an applied voltage of ±150

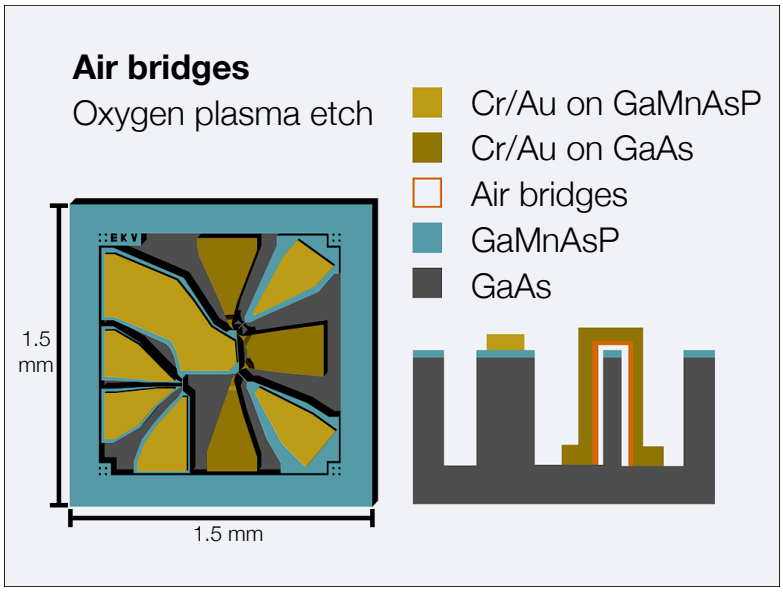


**Fig. 4.5.** Cartoon showing top-down and cross-section images of a fully-processed sample with CrAu bridge.

at 70 °C for 7 . Positive biasing voltages produced tensile strain along the aligned ($[1\bar{1}0]$ or [100]) axis, negative voltages produced compressive strain. Samples which are not pre-biased are cured at 70 °C for 7 . Previous work [53] used a higher curing temperature (120 °C for 2 hours) but concerns about reduced stressor function prompted the change in procedure to the above method.

The stressor is then end-mounted to a chip-carrier using flexible GE-varnish (to prevent any affect to stressor elongation/contraction). The sample contacts are Au wire-bonded to the chip carrier. The chip carrier is then attached to an oxygen-free copper sample holder and thermally anchored using GE-varnish and conductive silver-epoxy. The mounted sample is allowed to dry fully at room temperature (to prevent softening of the GE-varnish, as would occur during heated curing) prior to testing the electrical contacts. The sample holder is attached to an optical cryostat (Oxford Indstruments Microstat HR2).

## 4.3 Experimental Method

This study investigates the relationship between  motion and applied current in (Ga,Mn)(As,P) microbars. Following the results of previous one-dimensional (1D) simulations [53, 79], our model assumes an initial Bloch-type (or Néel) DW in perpendicularly-magnetized systems (e.g. (Ga,Mn)(As,P)) in which DW motion to be characterized by a low-current steady regime of viscous-flow, followed by the WB and then a higher-current precessional regime [39,40,74]. Of critical importances is the ratio of $\beta/\alpha$. In the case where $\beta/\alpha > 1$, the non-adiabatic  dominates and the DW mobility (the ratio of velocity, $v_{DW}$, to driving current, $j$) is higher below the WB. In the contrasting case, $\beta/\alpha < 1$, the mobility increases above the WB.

In order to test these predictions, our setup takes advantage of the fact that in (Ga,Mn)(As,P) as in (Ga,Mn)As the position of the WB can be manipulated by tuning the in-plane uniaxial magneto crystalline anisotropy field [50]. The dominant magnetic easy-axis for all of the samples is [001] (out-of-plane) and results from the tensile-strain induced by lattice mismatching between the (Ga,Mn)(As,P) epilayer and GaAs substrate. [80] Our experiments, however, focus on controlling the uniaxial in-plane mangeto-shape anisotropy, approximately 0.2 k/m$^3$ for a 25 nm thick $Ga_{0.94}Mn_{0.06}As_{0.91}P_{0.09}$ sample at 90  with magnetization $M \approx 18\,\mathrm{k}A/\mathrm{m}$, which is an order of magnitude smaller than the out-of-plane anisotropy. This can be accomplished by applying strain via the piezo-stressor, with the strength of the field controlled by the corresponding applied voltage [75, 79, 81]. The addition of the piezo-stressor strengthens the intrinsic in-plane uniaxial strain in (Ga,Mn)(As,P) along the $[1\bar{1}0]$ axis, due to the different thermal contraction of the stressor and GaAs substrate, amplifying usefulness of the technique even at zero applied voltage. Using this method, the DW mobility and critical current of the WB, $j_{\mathrm{WB}}$, can be systematically varied to determine the range of accessible $\beta/\alpha$ ratios in (Ga,Mn)(As,P). These limits characterize the relative contribution of the two mechanisms for gener-

ating STT in these materials (adiabatic vs non-adiabatic) for a range of experimental parameters.

### 4.3.1 Measurement setup

The sample holder is placed into an optical cryostat (Oxford Instruments Microstat HR2) and inserted into the MOKE spectroscopy apparatus. The cryostat is connected to a temperature controller (Keithley) which has a precision of 0.01 K and cooled by $^4$He vapor. The separation between the thermal sensor and the sample prevents the temperature at the sample surface from being directly measured. The temperature is therefore monitored using the 4-probe resistance of the sample and compared with a control measurement performed in a bath cryostat. [53]

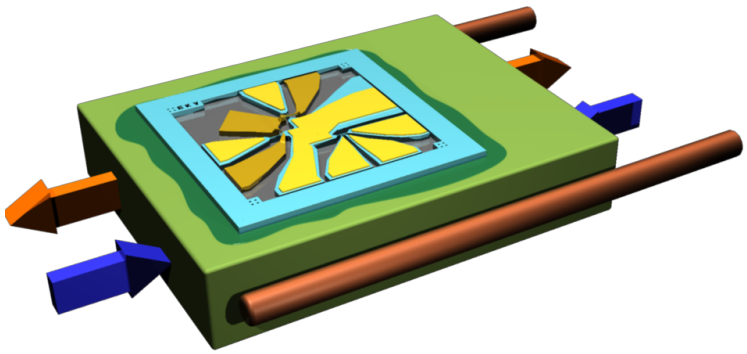

**Fig. 4.6.** Sample placed on a piezo actuator. Arrows denote direction of expansion (contraction)

The voltage applied to the piezo-stressor is controlled manually using an analog multi-source. This allows the rate of change to be continually adjusted to minimize leakage current (reducing damage to the stressor) while transitioning between volt-

ages (±200 V). (Fig. 4.6) The current pulses used to nucleate and push the DWs are generated by a digital multi-source and initiated manually.

The sample is illuminated using a mercury lamp (except during current pulses), and observed optically employing the polar magneto-optic Kerr effect, allowing real-time observation of the magnetic domain configuration. Due to the out-of-plane orientation of the magnetization in (Ga,Mn)(As,P), the MOKE system is set up such that the electromagnet can apply fields perpendicular to the sample surface. The electromagnet has a precision of 0.01 mT and is used in the range ±300 mT for these experiments. A camera connected to the ×50 microscope enables both video and still recordings of the sample. Vibration isolation techniques are used to minimize image noise.

### 4.3.2 Measurement techniques

After the sample is mounted, the cryostat is evacuated and slowly cooled to 90 K under increasing positive (negative) bias until reaching ± 200 V. The 4 probe resistivity measurement is used to monitor the temperature of the sample and is compared to a reference resistivity curve which was done using a sample from the same wafer in a bath cryostat. [53] The temperature is allowed to stabilize before measurements begin.

A reversed domain is nucleated in one of the microbars by sending a 10 μs current pulse of approximately 20 mA through the Au strip-line. Due to the sample geometry, one of the DWs is located in un-patterned 100 μm by 100 μm region of (Ga,Mn)(As,P), while the other DW is produced in the microbar. Thus, the DW in the microbar can be driven via current pulses, with out affecting the DW in the larger region, because the microbar has a much larger current density.

The magneto-crystalline anisotropy of (Ga,Mn)(As,P) produces a Bloch-type DW (perpendicular to the microbar) along the [110] microbar or a Néel-type (parallel) DW along the $[1\bar{1}0]$ bar (Fig. 4.7). The applied piezo strain is then used to modify

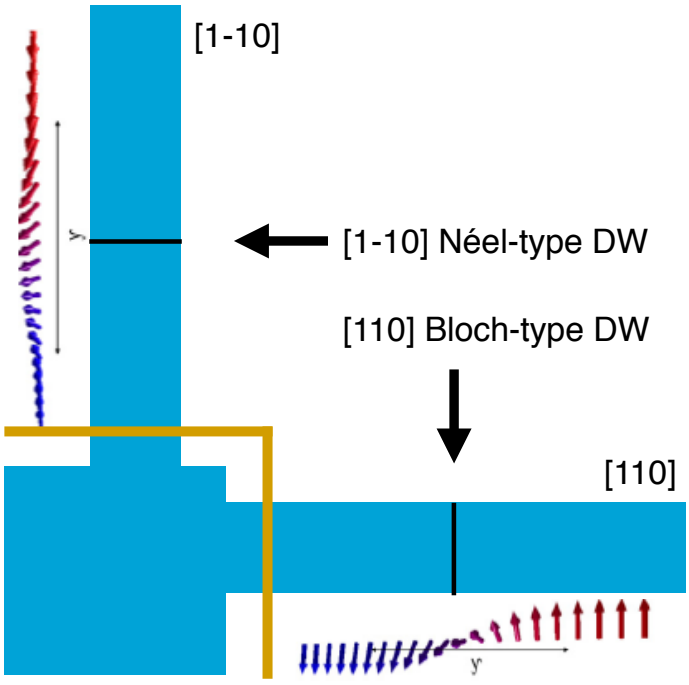


**Fig. 4.7.** Diagram of the types of DW nucleated in each sample

the anisotropy, stabilizing or destabilizing the DW, and affecting its mobility. (Néel DWs are known to propagate with higher velocities.) The results for each bar orientation are then compared.

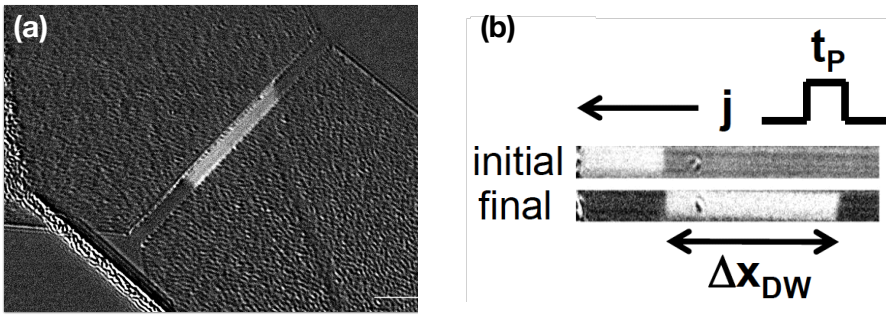


**Fig. 4.8.** **(a)** Sample micrograph of a magnetic domain nucleated in a microbar **(b)** Initial and final micrographs demonstrating DW propagation after a current pulse. [53]

Differential images are taken of the nucleated DW and its position after being driven by a 1 μs current pulse, using a MOKE micrograph (Fig. 4.8). A series of 10 of these pulses/differentials is used to determine the DW velocity and displacement for a particular current density. The series of measurements is repeated for a range of current densities for each microbar. The measurements are redone in both microbars using the same current densities under the opposite voltage bias $\mp$ 200 V. The resulting experimental data will be compared with theoretical calculations performed using the experimental parameters. The extracted DW velocities can then be used to analyze the role of the magneto-crystalline anisotropy in stabilizing/destabilizing a DW texture in each of the four bar orientations.

## 4.4 Results

This section discusses the experimental results, which confirm the viability of our method for fully-electric DW propagation. Systematic measurements of the DW motion were conducted for a range of driving current densities (Sec. 4.4.1). The resulting velocities were compared with the current density and used to determine the WB and critical current density, $j_{WB}$, as summarized in Section 4.4.2. The effect of applied compressive (tensile) piezo-strain is evaluated microbars oriented along [110] and [1$\bar{1}$0] as well as control measurement using [100] and [010] microbars.

### 4.4.1 Domain wall velocity

As outlined in the previous section, the DW velocity is determined by taking differential images of the position of the DW after a series of current pulses. The slope of this curve yields the corresponding velocity. An example of data taken for two values of current density is shown in Fig. 4.9. The smoothness of the slope between pulses suggests that we are in the flow regime (motion would be more stochastic in the extrinsic pinning/creep regime).

These experiments are then repeated for a total of ten pulses at each of a variety of current-density values. The resulting data are summarized in Fig. 4.10. As predicted by the magneto anisotropy, the more stable Bloch-type DWs occur in the [110] microbars, where both the in-plain magnetocrystalline anisotropy and the demagnetization field anisotropy support the formation of DWs with structure oriented perpendicular to the microbar direction. These Bloch structure exhibiting lower DW velocity. In the [1$\bar{1}$0] microbars, however, there is a strong competition between the magnetocrystalline anisotropy oriented along the [1$\bar{1}$0] easy axis, which favours the formation of a Néel-type structure and the demagnetization field shape anisotropy which favours a Bloch - structure where the magnetic moment rotation occurs perpendicular to the direction of the bar/propagation. Since the in-plane

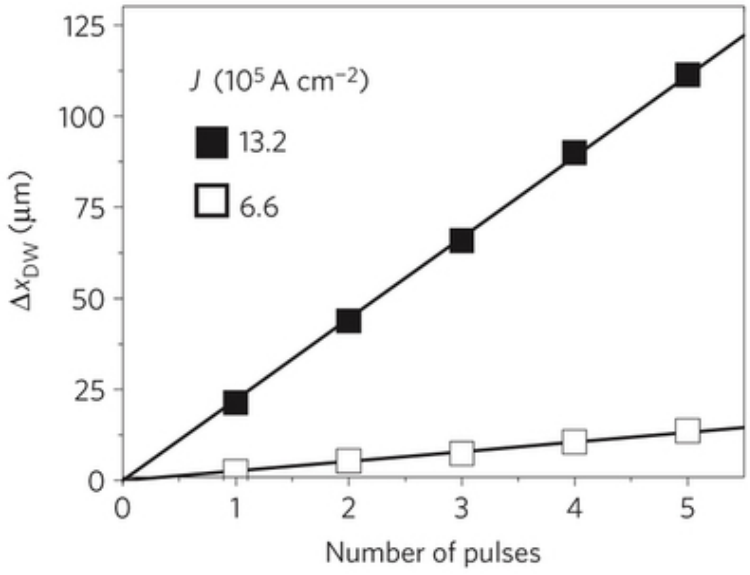


**Fig. 4.9.** Comparision of DW position with number of applied current pulses for two different current densities. The DW velocity can be taken as the slope of the curve. [53]

magnetocrystalline anisotropy field is stronger than the demagnetization field, the DW will take on the Néel-type internal structure. Such Néel-type DWs where the magnetic moment rotation occurs along the direction of the microbar/propagation, are more easily displaced than Blocl-type DWs. In addition, the competition weakens the stability of the DW in the $[1\bar{1}0]$ microbars.

### 4.4.2 Strain and the Walker breakdown

Beginning with the [110] bar under $-200$ V applied strain, we observe an initial linear relationship between the DW velocity and pulse current density. In this orientation, both the in-plane magnetocrystalline anisotropy and the demagnetizing field anisotropy support the formation of Bloch-type DW structures. Above $9.4 \times 10^9$ A/m$^2$, there is a sharp increase in the slope of the DW velocity, corresponding to the WB. The threshold current density required to overcome pinning effects ($3 \times 10^9$ A/m$^2$), motivated detailed measurements to confirm this change in $v_{DW}$ corresponds to the WB. For very low currents, the DW motion creeps between pinning sites, exhibiting non-linear behavior. (See supplement for Ref. [53]). As seen in Fig. 4.10, there is a clear shift in the position of the WB (and thus the critical current ($j_{WB}$) with the addition of applied strain.

We can easily identify the WB in the [110] sample data for the full range of positive and negative voltages (Fig. 4.10, right arrow). There is a clear shift of the WB from higher to lower current densities as the applied voltage changes from $-200$ V to $+200$ V. This is consistent with our theoretical picture, where the change from negative to positive voltages corresponds to a weakening of the anisotropy fields which stabilize Bloch-type DWs and the $[1\bar{1}0]$ in-plane easy axis (e.g. magnetocrystalline, demagnetizing). Thus reducing the internal stability of the Bloch-type DW, and shifting the WB to lower critical current densities. (Fig. 4.10)

The $[1\bar{1}0]$-oriented microbars favor the Néel-type DW structure, as the magnetocrystalline anisotropy along the $[1\bar{1}0]$ axis overcomes the contribution from the

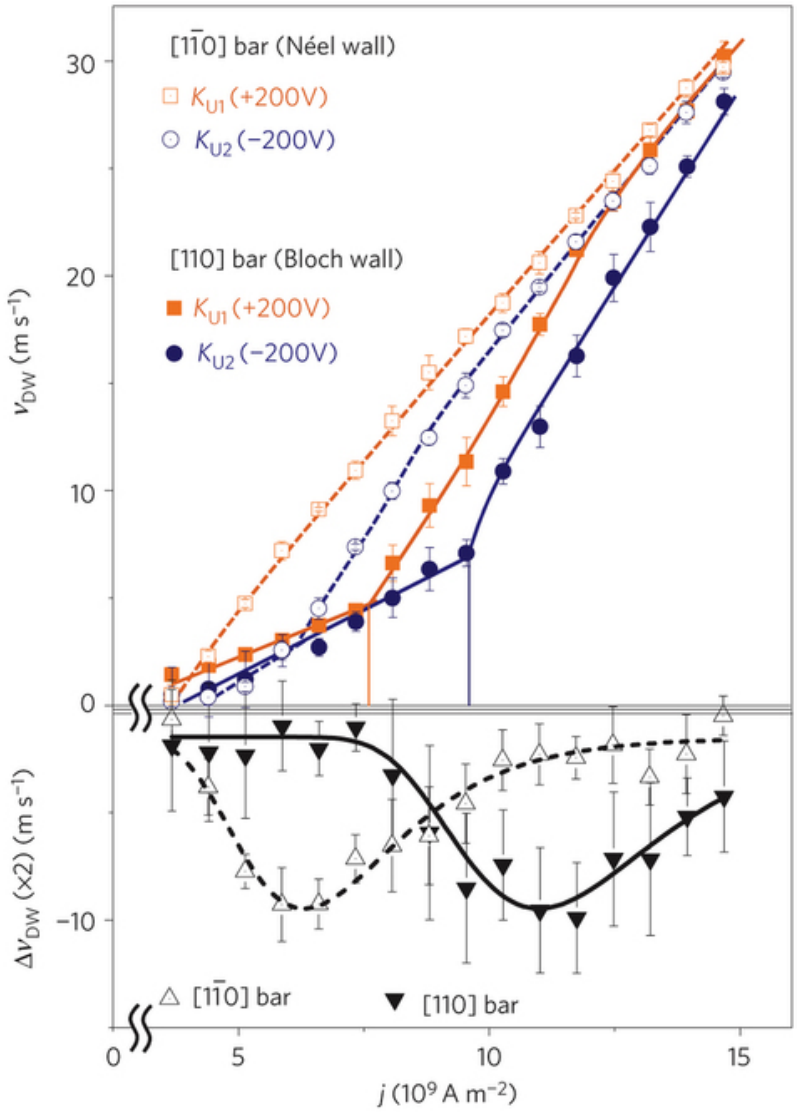


**Fig. 4.10. Top:** The DW velocity as a function of pulse current density for microbars oriented along [110] (filled symbols) and [1$\bar{1}$0] (unfilled symbols). Both positive and negative strains are shown for each bar, respectively strengthening (−200 V) or weakening the in-plane easy axis (along [1$\bar{1}$0]) **Bottom:** Change in DW velocity with change in the sign of the voltage applied to the piezo-stressor ($\pm$200 V $\rightarrow$ $\mp$200 V) plotted against current density. [53]

demagnetization field anisotropy. In the $[1\bar{1}0]$ microbar samples, a similar shift in the position of the WB occurs (Fig. 4.10, left arrow). It is more subtle to identify the shift in this orientation due to the low current density of the WBs for both current densities. This occurs due to the competition between the $[1\bar{1}0]$ magnetocrystalline anisotropy and the demagnetization field anisotropy of the Néel-type DW, which results in a comparatively less-stable DW structure (vs. the Bloch-type DW in the [110] oriented microbar).

Control measurements were completed in microbars oriented along [100] and [010] to evaluate DW velocities. In these samples the piezostrain applied along $[1\bar{1}0]$ axis should effect the DW structure in both bar orientations the same way, since they are symmetric with respect to the $[1\bar{1}0]$ easy axis anisotropy, such that neither Bloch nor Néel-type DWs are favoured. Thus resulting in identical DW velocities for the [100] and [010] microbar orientations as seen in Fig. 4.11. We note that the mobility of the control samples lies in between those of the strained [110] and $[1\bar{1}0]$ microbar orientations. These data are consistent with our picture of the effect of piezoelectric-induced strain on DW mobility in these materials.

Summarizing the above data, we find that the position of the WB shifts from the highest critical current dentisity in the [110] oriented samples, to an intermediate position for the [100] and [010] microbar orientations, and finally to the lowest critical current density in the $[1\bar{1}0]$ microbar samples. This shift can be understood by the competition of the in-plane magnetocrystalline anisotropy, demagnetizating field anisotropy, and additional contribution from the piezoelectric-induced strain. Furthermore, this dependences on crystal orientation provides evidence that even the lower current densities are within the flow regime - supporting the sharp change in DW mobility seen across the samples are indeed their respective WBs. These results verify that piezo-induced strain can be used to modify DW mobility by modifying the anisotropy fields which determine internal DW structure.

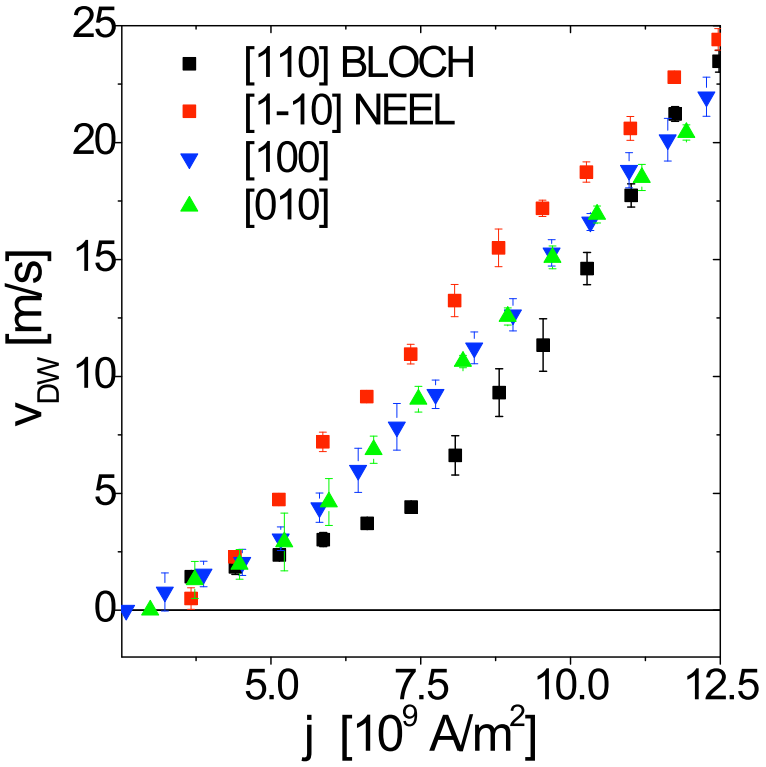


**Fig. 4.11.** Comparison of DW velocities for different microbars orientations under a piezo voltage of +200 V: a typical sample with microbars along [110] (black squares) and [1$\bar{1}$0] (red diamonds), and from a control sample with microbars oriented along [100] (blue downward triangles) and [010] (green upward triangles). The control sample data show no variation between the DW velocity for the two orientations under strain, as expected. NB: Strain is applied along the [1$\bar{1}$0] axis for both samples. Supp. [53]

# 5 CONCLUSIONS

The understanding of STT [21, 29, 38, 41, 42] and development of reliable, fully-electric, control mechanisms to manipulate magnetization [29, 43, 45, 47, 53] offer diverse avenues for developing new applications such as scalable, non-volatile logic and memory devices. These devices will account for the next generation of magnetic memory technology [59–61], however they are still limited by the complexity of the structures needed to generate and control STT.

Advances in the study of current-induced SOT in uniform systems [43–45, 82], may supersede these limitations allowing for less complex devices providing the same functionality. This thesis introduced SOT in the context of present STT literature, discussed its origins, and established the criteria necessary for SOT generation. This work extended the theory of SOT to include detailed relationships between material parameters (e.g. strain, shape, magnetization orientation) and current-induced SOFs and the resulting torque in ideal magnetic semiconductors (Ga,Mn)As and (Ga,Mn)(As,P). This model can be easily modified to describe a wide spectrum of DMSs, with the potential for SOT applications. The theoretical results presented here verify that the dominant contribution to SOT comes from the ISGE with small variations for magnetization orientation, supporting SOT as a viable mechanism for DW motion without altering the internal structure. Furthermore, systematic calculations covering a large area of parameter space were used to probe potentially interesting trends for future experiments.

Achieving fully-electric control of magnetic DWs is a key requirement of many novel logic and memory devices. The experiments discussed in this thesis establish a mechanism for precise control over electrically-driven DW mobility via a piezoelectric actuator (stressor), modifying the DW velocity in-situ. The direct observation and manipulation of DW velocity as well as the critical current density at which the WB occurs, makes this technique a valuable lens in the study of the phe-

nomena regulating DW motion. In addition to the quintessential (Ga,Mn)As and (Ga,Mn)(As,P) discussed herein, this method has the potential for use in diverse materials, including other magnetic semiconductors and ferromagnetic systems with strong SOC and minimal extrinsic DW pinning effects. In combination with the theoretical calculations, these experiments present a powerful tool for understanding and controlling DW propagation in uniform ferromagnetic microstructures.

Future directions for investigations beyond this thesis are plentiful. One primary opportunity lies in expanding the study to related materials, particularly the search for these phenomena in room-temperature ferromagnetic metals. The demonstration of current-induced SOT control over magnetic domains in a room temperature material would have significant impact on new memory and logic technologies. Similarly, detailed investigations of the of competition between adiabatic and non-adiabatic STTs and the relationship to various material parameters could further the basic understanding of DW propagation.

Another interesting course is to devise an experimental method of observing the influence of current-induced SOFs. By applying strain along either the [100] or [010] crystalline axis and comparing the resulting DW mobility curves for microbars patterned along the [110] and $[1\bar{1}0]$ directions, one might be able to measure the relative strengths of the Dresselhaus-symmetric growth strain ($\epsilon_{xx}$) and and the Rashba-symmetric shear strain ($\epsilon_{xy}$) strain. Along one sample orientation the two terms will add together, and on the other they will oppose (the relative orientation of the Rashba term to is the same with respect to [110] and $[1\bar{1}0]$ microbars, whereas the relative orientation of the Dresselhaus term switches). This would allow an indirect measurement of twice the difference in magnitude of the component fields.

A third option is to modify the theoretical model to include more experimental details such as temperature dependence. This would enable more detailed comparisons with experiments which can be performed over a range of temperatures, [45] and allowing an additional means of checking the theoretical results using temper-

ature dependence of individual components of the calculations, (e.g. conductivity, magnetization). The inclusion of additional electronic bands may also show additional physics, although precise first principles calculations of some of the constants would be required before such changes could be made.

The results of the work comprising this thesis strongly support SOT and applied piezo-strain as two potential control mechanisms for nonvolatile logic and memory devices. Taking advantage of the rich, tunable, degrees of freedom in materials with strong SOC and inversion asymmetry, such as using strain, to manipulate DWs takes a step closer to realizing the fully-electric, room-temperature, memory elements necessary for integrated logic and memory devices. These same devices which promise to supersede the limitations of current technologies, and offer solutions to the demand for energy-conscious, smaller, faster personal electronic devices.

# REFERENCES


[1] H. Ohno, H. Munekata, T. Penney, S. von Molnár, and L. L. Chang, "Magnetotransport properties of p -type (In,Mn)As diluted magnetic III-V semiconductors", Phys. Rev. Lett., 68, 2664–2667 (1992).

[2] H. Ohno, A. Shen, F. Matsukura, A. Oiwa, A. Endo, S. Katsumoto, and Y. Iye, "(Ga,Mn)As: A new diluted magnetic semiconductor based on GaAs", App. Phys. Lett., 69, 363–365 (1996).

[3] L. Burns, "Applications for GaAs and silicon integrated circuits in next generation wireless communication systems", IEEE J. Sol. Stat. Circ., 30, 1088–1095 (1995).

[4] D. Desimone, C. E. C. Wood, and C. A. Evans, Jr., "Manganese incorporation behavior in molecular beam epitaxial gallium arsenide", J. App. Phys., 53, 4938–4942 (1982).

[5] A. Casiraghi, "Manipulating the magnetic anisotropy in the ferromagnetic semiconductor Gallium Manganese Arsenide", Ph.D. thesis, University of Nottingham, Nottingham, UK (2012).

[6] H. Ohno, "Making Nonmagnetic Semiconductors Ferromagnetic", Science, 281, 951–956 (1998).

[7] R. Campion, K. Edmonds, L. Zhao, K. Wang, C. Foxon, B. Gallagher, and C. Staddon, "High-quality GaMnAs films grown with arsenic dimers", J. Crys. Grow., 247, 42 – 48 (2003).

[8] P. W. Anderson, "Antiferromagnetism. Theory of Superexchange Interaction", Phys. Rev., 79, 350–356 (1950).

[9] C. Zener, "Interaction Between the d Shells in the Transition Metals", Phys. Rev., 81, 440–444 (1951).

[10] T. Dietl, H. Ohno, F. Matsukura, J. Cibert, and D. Ferrand, "Zener Model Description of Ferromagnetism in Zinc-Blende Magnetic Semiconductors", Science, 287, 1019–1022 (2000).

[11] P. Nemec, V. Novák, N. Tesarová, E. Rozkotová, H. Reichlová, D. Butkovicová, F. Trojánek, K. Olejnik, P. Malý, R. P. Campion, B. L. Gallagher, J. Sinova, and T. Jungwirth, "The essential role of carefully optimized synthesis for elucidating intrinsic material properties of (Ga,Mn)As", Nature Communications, 4 (2013).

[12] K. M. Yu, W. Walukiewicz, T. Wojtowicz, I. Kuryliszyn, X. Liu, Y. Sasaki, and J. K. Furdyna, "Effect of the location of Mn sites in ferromagnetic $Ga_{1-x}Mn_xAs$ on its Curie temperature", Phys. Rev. B, 65, 201303 (2002).

[13] K. W. Edmonds, K. Y. Wang, R. P. Campion, A. C. Neumann, N. R. S. Farley, B. L. Gallagher, and C. T. Foxon, "High-Curie-temperature $Ga_{1-x}Mn_xAs$ obtained by resistance-monitored annealing", App. Phys. Lett., 81 (2002).

[14] K. W. Edmonds, P. Bogusawski, K. Y. Wang, R. P. Campion, S. N. Novikov, N. R. S. Farley, B. L. Gallagher, C. T. Foxon, M. Sawicki, T. Dietl, M. Buongiorno Nardelli, and J. Bernholc, "Mn Interstitial Diffusion in (Ga,Mn)As", Phys. Rev. Lett., 92, 037201 (2004).

[15] K. W. Edmonds, N. R. S. Farley, T. K. Johal, G. van der Laan, R. P. Campion, B. L. Gallagher, and C. T. Foxon, "Ferromagnetic moment and antiferromagnetic coupling in (Ga,Mn)As thin films", Phys. Rev. B, 71, 064418 (2005).

[16] Y. K. Kato and D. D. Awschalom, "Electrical Manipulation of Spins in Nonmagnetic Semiconductors", J. Phys. Soc. Jpn., 77, 031006 (2008).

[17] R. Haug (Editor), Advances in Solid State Physics, vol. 49, Springer-Verlag, Berlin (2010).

[18] A. G. Aronov and Y. B. Lyanda-Geller, "Nuclear electric resonance and orientation of carrier spins by an electric field", JETP Lett., 50, 431 (1989).

[19] V. M. Edelstein, "Spin polarization of conduction electrons induced by electric current in two-dimensional asymmetric electron systems", Sol. Stat. Comm., 73, 233 – 235 (1990).

[20] S. D. Ganichev, E. L. Ivchenko, V. V. Belkov, S. A. Tarasenko, M. Sollinger, D. Weiss, W. Wegscheider, and W. Prettl, "Spin-galvanic effect", Nature, 417, 153 –156 (2002).

[21] H. Kurebayashi, J. Sinova, D. Fang, A. C. Irvine, J. Wunderlich, V. Novak, R. P. Campion, B. L. Gallagher, E. K. Vehstedt, L. P. Zarbo, K. Vyborny, A. J. Ferguson, and T. Jungwirth, "Observation of a Berry phase anti-damping spin-orbit torque", Nat. Nano., 9, 211–217 (2014).

[22] I. Garate and A. H. MacDonald, "Influence of a transport current on magnetic anisotropy in gyrotropic ferromagnets", Phys. Rev. B, 80, 134403 (2009).

[23] I. Garate, K. Gilmore, M. D. Stiles, and A. H. MacDonald, "Nonadiabatic spin-transfer torque in real materials", Phys. Rev. B, 79, 104416 (2009).

[24] G. C. La Rocca, N. Kim, and S. Rodriguez, "Effect of uniaxial stress on the electron spin resonance in zinc-blende semiconductors", Phys. Rev. B, 38, 7595–7601 (1988).

[25] F. G. Pikus and G. E. Pikus, "Conduction-band spin splitting and negative magnetoresistance in A3B5 heterostructures", Phys. Rev. B, 51, 16928–16935 (1995).

[26] G. L. Bir and G. E. Pikus, Symmetry and strain-induced effects in semiconductors, Wiley, New York (1974).

[27] Y. E. Zhu, Modern Techniques for Characterizing Magnetic Materials, Springer, New York (2005).

[28] I. L. Prejbeanu, M. Kerekes, R. C. Sousa, H. Sibuet, O. Redon, B. Dieny, and J. P. Nozieres, "Thermally assisted MRAM", J. Phys.: Cond. Matt., 19, 165218 (2007).

[29] D. Ralph and M. Stiles, "Spin transfer torques", J. Mag. Magn. Mat., 320, 1190 – 1216 (2008).

[30] C. Chappert, A. Fert, and F. N. Van Dau, "The emergence of spin electronics in data storage", Nat. Mater, 6, 813–823 (2007).

[31] F. Matsukura, H. Ohno, and T. Dietl, Handbook of Magnetic Materials, vol. 14, Elsevier, Amsterdam (2002).

[32] T. Jungwirth, J. Sinova, J. Masek, J. Kucera, and A. H. MacDonald, "Theory of ferromagnetic (III,Mn)V semiconductors", Rev. Mod. Phys., 78, 809–864 (2006).

[33] S. Zhang and Z. Li, "Roles of Nonequilibrium Conduction Electrons on the Magnetization Dynamics of Ferromagnets", Phys. Rev. Lett., 93, 127204 (2004).

[34] A. Vanhaverbeke and M. Viret, "Simple model of current-induced spin torque in domain walls", Phys. Rev. B, 75, 024411 (2007).

[35] J. Fernández-Rossier, A. S. Núñez, M. Abolfath, and A. H. MacDonald, "Optical spin transfer in ferromagnetic semiconductors", eprint arXiv:cond-mat/0304492 (2003).

[36] P. Nemec, E. Rozkotova, N. Tesarova, F. Trojanek, E. De Ranieri, K. Olejnik, J. Zemen, V. Novak, M. Cukr, P. Maly, and T. Jungwirth, "Experimental observation of the optical spin transfer torque", Nat. Phys., 8, 411–415 (2012).

[37] J. C. Slonczewski, "Current-driven excitation of magnetic multilayers", J. Mag. Magn. Mat., 159, L1 – L7 (1996).

[38] L. Berger, "Emission of spin waves by a magnetic multilayer traversed by a current", Phys. Rev. B, 54, 9353–9358 (1996).

[39] P. J. Metaxas, J. P. Jamet, A. Mougin, M. Cormier, J. Ferré, V. Baltz, B. Rodmacq, B. Dieny, and R. L. Stamps, "Creep and Flow Regimes of Magnetic Domain-Wall Motion in Ultrathin Pt/Co/Pt Films with Perpendicular Anisotropy", Phys. Rev. Lett., 99, 217208 (2007).

[40] A. Mougin, M. Cormier, J. P. Adam, P. J. Metaxas, and J. Ferre, "Domain wall mobility, stability and Walker breakdown in magnetic nanowires", Europhys. Lett., 78, 57007 (2007).

[41] A. Manchon and S. Zhang, "Theory of nonequilibrium intrinsic spin torque in a single nanomagnet", Phys. Rev. B, 78, 212405 (2008).

[42] A. Manchon and S. Zhang, "Theory of spin torque due to spin-orbit coupling", Phys. Rev. B, 79, 094422 (2009).

[43] A. Chernyshov, M. Overby, X. Liu, J. K. Furdyna, Y. Lyanda-Geller, and L. P. Rokhinson, "Evidence for reversible control of magnetization in a ferromagnetic material by means of spin-orbit magnetic field", Nat. Phys., 5, 656–659 (2009).

[44] I. M. Miron, G. Gaudin, S. Auffret, B. Rodmacq, A. Schuhl, S. Pizzini, J. Vogel, and P. Gambardella, "Current-driven spin torque induced by the Rashba effect in a ferromagnetic metal layer", Nat. Mater., 9, 230–234 (2010).

[45] D. Fang, H. Kurebayashi, J. Wunderlich, K. Vyborny, L. P. Zarbo, R. P. Campion, A. Casiraghi, B. L. Gallagher, T. Jungwirth, and A. J. Ferguson, "Spin-orbit-driven ferromagnetic resonance", Nat. Nano., 6, 413–417 (2011).

[46] P. Gambardella and I. M. Miron, "Current-induced spin-orbit torques", Phil. Trans. R. Soc. A, 369, 3175–3197 (2011).

[47] D. Fang, "Current-Induced Torque Driven Ferromagnetic Resonance in Magnetic Microstructures", Ph.D. thesis, University of Cambridge, Cambridge, UK (2009).

[48] I. M. Miron, T. Moore, H. Szambolics, L. D. Buda-Prejbeanu, S. Auffret, B. Rodmacq, S. Pizzini, J. Vogel, M. Bonfim, A. Schuhl, and G. Gaudin, "Fast current-induced domain-wall motion controlled by the Rashba effect", Nat. Mater., 10, 419–423 (2011).

[49] H. Ohno and T. Dietl, "Spin-transfer physics and the model of ferromagnetism in (Ga,Mn)As", J. Mag. Magn. Mat., 320, 1293 – 1299 (2008).

[50] J. Zemen, J. Kucera, K. Olejnik, and T. Jungwirth, "Magnetocrystalline anisotropies in (Ga,Mn)As: Systematic theoretical study and comparison with experiment", Phys. Rev. B, 80, 155203 (2009).

[51] M. Abolfath, T. Jungwirth, J. Brum, and A. H. MacDonald, "Theory of magnetic anisotropy in III1-xMnxV ferromagnets", Phys. Rev. B, 63, 054418 (2001).

[52] M. Silver, W. Batty, A. Ghiti, and E. P. O'Reilly, "Strain-induced valence-subband splitting in III-V semiconductors", Phys. Rev. B, 46, 6781–6788 (1992).

[53] E. De Ranieri, P. E. Roy, D. Fang, E. K. Vehstedt, A. C. Irvine, D. Heiss, A. Casiraghi, R. P. Campion, B. L. Gallagher, T. Jungwirth, and J. Wunderlich, "Piezoelectric control of the mobility of a domain wall driven by adiabatic and non-adiabatic torques", Nat. Mater., 12, 808–814 (2013).

[54] S. I. Kiselev, J. C. Sankey, I. N. Krivorotov, N. C. Emley, R. J. Schoelkopf, R. A. Buhrman, and D. C. Ralph, "Microwave oscillations of a nanomagnet driven by a spin-polarized current", Nature, 425, 380 – 383 (2003).

[55] J. Akerman, "Toward a Universal Memory", Science, 308, 508–510 (2005).

[56] J. C. Sankey, I. N. Krivorotov, S. I. Kiselev, P. M. Braganca, N. C. Emley, R. A. Buhrman, and D. C. Ralph, "Mechanisms limiting the coherence time of spontaneous magnetic oscillations driven by dc spin-polarized currents", Phys. Rev. B, 72, 224427 (2005).

[57] A. A. Tulapurkar, Y. Suzuki, A. Fukushima, H. Kubota, H. Maehara, K. Tsunekawa, D. D. Djayaprawira, N. Watanabe, and S. Yuasa, "Spin-torque diode effect in magnetic tunnel junctions", Nature, 438, 339–342 (2005).

[58] J. C. Sankey, P. M. Braganca, A. G. F. Garcia, I. N. Krivorotov, R. A. Buhrman, and D. C. Ralph, "Spin-Transfer-Driven Ferromagnetic Resonance of Individual Nanomagnets", Phys. Rev. Lett., 96, 227601 (2006).

[59] Y. Huai, "Spin-transfer torque MRAM (STT-MRAM): Challenges and prospects", AAPPS Bulletin, 18, 33–40 (2008).

[60] M. Hayashi, L. Thomas, R. Moriya, C. Rettner, and S. S. P. Parkin, "Current-Controlled Magnetic Domain-Wall Nanowire Shift Register", Science, 320, 209–211 (2008).

[61] S. S. P. Parkin, M. Hayashi, and L. Thomas, "Magnetic Domain-Wall Racetrack Memory", Science, 320, 190–194 (2008).

[62] E. B. Myers, D. C. Ralph, J. A. Katine, R. N. Louie, and R. A. Buhrman, "Current-Induced Switching of Domains in Magnetic Multilayer Devices", Science, 285, 867–870 (1999).

[63] F. J. Albert, J. A. Katine, R. A. Buhrman, and D. C. Ralph, "Spin-polarized current switching of a Co thin film nanomagnet", App. Phys. Lett., 77, 3809–3811 (2000).

[64] J. A. Katine, F. J. Albert, R. A. Buhrman, E. B. Myers, and D. C. Ralph, "Current-Driven Magnetization Reversal and Spin-Wave Excitations in Co /Cu /Co Pillars", Phys. Rev. Lett., 84, 3149–3152 (2000).

[65] S. I. Kiselev, J. C. Sankey, I. N. Krivorotov, N. C. Emley, A. G. F. Garcia, R. A. Buhrman, and D. C. Ralph, "Spin-transfer excitations of permalloy nanopillars for large applied currents", Phys. Rev. B, 72, 064430 (2005).

[66] M. Hayashi, L. Thomas, C. Rettner, R. Moriya, Y. B. Bazaliy, and S. S. P. Parkin, "Current Driven Domain Wall Velocities Exceeding the Spin Angular Momentum Transfer Rate in Permalloy Nanowires", Phys. Rev. Lett., 98, 037204 (2007).

[67] M. Yamanouchi, D. Chiba, F. Matsukura, and H. Ohno, "Current-induced domain-wall switching in a ferromagnetic semiconductor structure", Nature, 428, 539 – 542 (2004).

[68] M. Yamanouchi, J. Ieda, F. Matsukura, S. E. Barnes, S. Maekawa, and H. Ohno, "Universality Classes for Domain Wall Motion in the Ferromagnetic Semiconductor (Ga,Mn)As", Science, 317, 1726–1729 (2007).

[69] J. Wunderlich, A. C. Irvine, J. Zemen, V. Holý, A. W. Rushforth, E. De Ranieri, U. Rana, K. Výborný, J. Sinova, C. T. Foxon, R. P. Campion, D. A. Williams, B. L. Gallagher, and T. Jungwirth, "Local control of magnetocrystalline anisotropy in (Ga,Mn)As microdevices: Demonstration in current-induced switching", Phys. Rev. B, 76, 054424 (2007).

[70] K. M. D. Hals, A. K. Nguyen, and A. Brataas, "Intrinsic Coupling between Current and Domain Wall Motion in (Ga,Mn)As", Phys. Rev. Lett., 102, 256601 (2009).

[71] J.-P. Adam, N. Vernier, J. Ferré, A. Thiaville, V. Jeudy, A. Lemaˆ, L. Thevenard, and G. Faini, "Nonadiabatic spin-transfer torque in (Ga,Mn)As with perpendicular anisotropy", Phys. Rev. B, 80, 193204 (2009).

[72] J. Curiale, A. Lemâ, C. Ulysse, G. Faini, and V. Jeudy, "Spin Drift Velocity, Polarization, and Current-Driven Domain-Wall Motion in (Ga,Mn)(As,P)", Phys. Rev. Lett., 108, 076604 (2012).

[73] M. Yamanouchi, D. Chiba, F. Matsukura, T. Dietl, and H. Ohno, "Velocity of Domain-Wall Motion Induced by Electrical Current in the Ferromagnetic Semiconductor (Ga,Mn)As", Phys. Rev. Lett., 96, 096601 (2006).

[74] A. Thiaville, Y. Nakatani, J. Miltat, and Y. Suzuki, "Micromagnetic understanding of current-driven domain wall motion in patterned nanowires", Europhys. Lett., 69, 990–996 (2005).

[75] A. W. Rushforth, M. Wang, N. R. S. Farley, R. P. Campion, K. W. Edmonds, C. R. Staddon, C. T. Foxon, and B. L. Gallagher, "Molecular beam epitaxy grown (Ga,Mn)(As,P) with perpendicular to plane magnetic easy axis", J. App. Phys., 104, 073908 (2008).

[76] A. Casiraghi, A. W. Rushforth, M. Wang, N. R. S. Farley, P. Wadley, J. L. Hall, C. R. Staddon, K. W. Edmonds, R. P. Campion, C. T. Foxon, and B. L. Gallagher, "Tuning perpendicular magnetic anisotropy in (Ga,Mn)(As,P) by thermal annealing", App. Phys. Lett., 97, 122504 (2010).

[77] E. De Ranieri, A. W. Rushforth, K. Výborný, U. Rana, E. Ahmad, R. P. Campion, C. T. Foxon, B. L. Gallagher, A. C. Irvine, J. Wunderlich, and T. Jungwirth, "Lithographically and electrically controlled strain effects on anisotropic magnetoresistance in (Ga,Mn)As", New Journal of Physics, 10, 065003 (2008).

[78] E. De Ranieri, "Strain-induced effects on the magnetotransport proper- ties of GaMnAs diluted magnetic semiconductors", Ph.D. thesis, University of Cambridge, Cambridge, UK (2009).

[79] P. E. Roy and J. Wunderlich, "In-plane magnetic anisotropy dependence of critical current density, Walker field and domain-wall velocity in a stripe with perpendicular anisotropy", App. Phys. Lett., 99, 122504 (2011).

[80] X. Liu and J. K. Furdyna, "Ferromagnetic resonance in $Ga_{1-x}Mn_xAs$ dilute magnetic semiconductors", J. Phys.: Cond. Mat., 18, R245 (2006).

[81] G. Tatara, T. Takayama, H. Kohno, J. Shibata, Y. Nakatani, and H. Fukuyama, "Threshold Current of Domain Wall Motion under Extrinsic Pinning, $\beta$-Term and Non-Adiabaticity", J. Phys. Soc. Jpn., 75, 064708 (2006).

[82] U. H. Pi, K. Won Kim, J. Y. Bae, S. C. Lee, Y. J. Cho, K. S. Kim, and S. Seo, "Tilting of the spin orientation induced by Rashba effect in ferromagnetic metal layer", App. Phys. Lett., 97, 162507 (2010).

# APPENDIX A
# ABBREVIATIONS AND NOMENCLATURE

## Acronyms and Initialisms

**2DEG** two-dimensional electron gas

**DMS** dilute magnetic semiconductor

**DW** domain wall

**e-beam** electron beam

**ISGE** inverse spin-galvanic effect

**LT - MBE** low-temperature molecular beam epitaxy

**MBE** molecular beam epitaxy

**MOKE** magneto-optic Kerr effect

**MRAM** magnetoresistive random access memory

**RIE** reactive ion etching

**SO** spin-orbit

**SOC** spin-orbit coupling

**SOF** spin-orbit field

**SOI** spin-orbit interaction

**SOT** spin-orbit torque

**SQUID** superconducting quantum interference device

**STT** spin-transfer torque

**STT-MRAM** spin-transfer torque magnetic random access memory

**WB** Walker breakdown

Chemical Abbreviations

**DI-water** de-ionized water

**GaAs** gallium arsenide

**(Ga,Mn)As** gallium manganese arsenide

**(Ga,Mn)(As,P)** gallium manganese arsenide phosphate

**IPA** isopropyl alcohol

**MIBK** methyl isobutyl ketone

**PMMA** polymethylmethacrylate

# APPENDIX B

# FABRICATION PARAMETERS

**Annealing**

1. Remove protective PMMA from chips with acetone for 5 minutes
2. Rinse: IPA for 5 minutes and dry with $N_2$ gas
3. Anneal: 180 °C in air for 48 hours

**Mesa**

1. Resist: spin A8 PMMA (950 mw) for 1 minute at 5000 rpm / 45 acc.
2. Cure: 120 °C for 1 hour
3. E-beam: 650 C/cm$^2$ exposure (A. Irvine, D. Heiss)
4. Develop: MIBK:IPA (1:3) for 1 minute
5. Rinse: IPA (1 minute) and dry with $N_2$ gas
6. Oxygen plasma: 30 seconds
7. Reactive ion etching: 120 seconds with $SiCl_4$ and Ar gas mixture
8. Rinse: acetone for 1 minute IPA for 30 seconds and dry with $N_2$ gas

**Cross-linking**

1. Resist: spin A4 PMMA (950 mw) for 45 s at 5000 rpm / 45 acc. (180 $\mu$m thick)
2. E-beam: 850 C/cm$^2$
3. Remove PMMA from chips with acetone for 5 minutes
4. Rinse: IPA for 30 seconds and dry with $N_2$ gas

**Metalization**

1. Resist: spin A8 PMMA (950 mw) for 1 minute at 5000 rpm / 45 acc.
2. Cure: 120 °C for 1 hour

3. E-beam: 650 C/cm$^2$ exposure (A. Irvine, D. Heiss)
4. Develop: MIBK:IPA (1:3) for 1 minute
5. Rinse: IPA (1 minutes) and dry with $N_2$ gas
6. Oxygen plasma: 30 seconds
7. Clean: HCl%:$H_2O$ (1:10) for 30 s
8. Rinse: DI-water 30 seconds and dry with $N_2$ gas
9. Deposition: 20 nm Cr at 4.2 Å/s, 280 nm Au 2.2 Å/s
10. Lift-off: acetone bath until Au can be easily removed (2 - 5 hours)
11. Rinse: IPA for 30 seconds and dry with $N_2$ gas

**Remove Cross-linked PMMA**

1. Oxygen plasma: 30 minutess

**Thinning**

1. Grinding: Gatlan 623 Disc Grinder
2. Lapping pads: Buehler TexMet and VerduTex polishing cloths
3. Suspensions: MedaDi Supreme, polycrystaline diamond suspensions

**Stressors**

1. Stressors: 2 mm $\times$ 3 mmx3 mm Piezo-electric actuators Piezomechanik GmbH
2. Epoxy: Vishay M-Bond 600 epoxy
3. Varnish: GE Varnish (IMI-7031)

# APPENDIX C

# COMPUTATIONAL PARAMETERS

The methods discussed in this thesis were used to calculate the current-induced SOF for a wide range of parameters. The breadth of the work prevented a detailed discussion of the full parameter space here. A summary of the parameters used in additional calculations can be found in Table C.1. Simulations were run for all parameter combinations

**Table C.1**
Parameters used to calculate current-induced SOF in $Ga_{1-x}Mn_xAs_{1-y}P_y$

| Parameter | Symbol | Units | Values |
|---|---|---|---|
| Crystal (microbar) orientation | | [xyz] | [100], [110], [010], [$1\bar{1}0$] |
| Hole (carrier) compensation | $c$ | 0.x | 0, 1, 2, 3, 4, 5, 6, 7, 8, 9, 10 |
| Hole (carrier) density | $p$ | $nm^{-3}$ | p=0.22*c*x*100 |
| Luttinger parameters | $\gamma_i$ | | regular ($\gamma_1 \neq \gamma_2 \neq \gamma_3$)<br>spherical ($\gamma_1 \neq \gamma_2 = \gamma_3$)<br>parabolic ($\gamma_1,\ \gamma_2 = \gamma_3 = 0$) |
| Magnetization angle (vs [100]) | $\phi$ | rad. | (0,2$\pi$), step = $\pi/32$ |
| Magnetization (vs current) | $\theta$ | rad. | (0,2$\pi$), step = $\pi/32$ |
| Mn substitutional fraction | $x$ | 0.0x (%) | 0, 3, 4, 5, 6, 7, 8, 9, 12 |
| P substitutional fraction | $y$ | 0.0y (%) | 0, 9 |
| Spectral broadening | $\Gamma$ | meV | 25, 50, 75, 100 |
| Strain (growth) | $\epsilon_{xx}$ | % | $0.0, \pm0.1, \pm0.3, \pm1.0, \pm3.0$ |
| Strain (shear) | $\epsilon_{xy}$ | % | $0.0, \pm0.1, \pm0.3, \pm1.0, \pm3.0$ |
| Strain relaxation | $\rho$ | | [100] $\rho$=0.58, [110] $\rho$=0.47 |

# APPENDIX D
# CONTRIBUTIONS

This thesis discusses the results of theoretical and experimental research performed by E.K.V.. The projects are part of a large-scale collaboration between groups at Texas A&M University, the Academy of Sciences of the Czech Republic, the Hitachi Cambridge Laboratory, the University of Cambridge, and the University of Nottingham. The collaborator contributions are listed below in alphabetical order.

The theory was developed by T.J., J.S., E.K.V., K.V., and L.P.Z.; E.K.V. performed the modeling. R.P.C. and B.L.G. grew and provided the (Ga,Mn)(As,P) thin films. A.C., E.D.R., and D.F. performed magnetic characterizations of the DW devices and un-patterned films. E.D.R., A.C.I., E.K.V., and J.W. designed the devices. C.C., E.D.R., D.H., A.C.I., and E.K.V. fabricated the samples. E.D.R., P.E.R., E.K.V., and J.W., developed the DW experimental set-up. E.D.R. and E.K.V. performed the DW measurements. E.D.R., T.J., P.E.R., E.K.V. and J.W. performed the data analysis. P.E.R. performed micro magnetic simulations (see Ref. [53]).

Additional experiments studying spin-orbit driven ferromagnetic resonance in (Ga,Mn)As and (Ga,Mn)(As,P) were developed in conjunction with the projects herein and provided key information and discussions relevant to this work [21, 45]. R.P.C., B.L.G., and V.N. prepared the materials. D.F.,A.J.F., and A.C.I. performed the sample fabrication. D.F., A.J.F., H.K., and J.W. carried out the experiments and data analysis. T.J., J.S., E.K.V., K.V., and L.P.Z. performed the theoretical modeling.

Collaborators

**R.P.C.** Richard P. Campion, School of Physics and Astronomy, University of Nottingham, Nottingham NG7 2RD, United Kingdom

**A.C.** Arianna Casiraghi, School of Physics and Astronomy, University of Nottingham, Nottingham NG7 2RD, United Kingdom

**C.C.** Chiara Ciccarelli, Cavendish Laboratory, University of Cambridge, J.J. Thomson Avenue, CB3 0HE, United Kingdom

**E.D.R.** Elisa De Ranieri, Hitachi Cambridge Laboratory, Cambridge CB3 0HE, United Kingdom

**D.F.** Dong Fang, Cavendish Laboratory, University of Cambridge, J.J. Thomson Avenue, CB3 0HE, United Kingdom

**A.J.F.** Andrew J. Ferguson, Cavendish Laboratory, University of Cambridge, J.J. Thomson Avenue, CB3 0HE, United Kingdom

**B.L.G.** Bryan C. Gallagher, School of Physics and Astronomy, University of Nottingham, Nottingham NG7 2RD, United Kingdom

**D.H.** Dominic Heiss, Cavendish Laboratory, University of Cambridge, J.J. Thomson Avenue, CB3 0HE, United Kingdom

**A.C.I.** Andrew C. Irvine, Cavendish Laboratory, University of Cambridge, J.J. Thomson Avenue, CB3 0HE, United Kingdom

**T.J.** Tomas Jungwirth, Institute of Physics ASCR, v.v.i., Cukrovarnická 10, 162 53 Praha 6, Czech Republic and School of Physics and Astronomy, University of Nottingham, Nottingham NG7 2RD, United Kingdom

**H.K.** Hidekazu Kurebayashi, Cavendish Laboratory, University of Cambridge, J.J. Thomson Avenue, CB3 0HE, United Kingdom

**V.N.** Vit Novák, Institute of Physics ASCR, v.v.i., Cukrovarnická 10, 162 53 Praha 6, Czech Republic

**P.E.R.** Piere E. Roy, Hitachi Cambridge Laboratory, Cambridge CB3 0HE, United Kingdom

**J.S.** Jairo Sinova, Department of Physics, Texas A&M University, College Station, Texas 77843-4242, USA, Institute of Physics ASCR, v.v.i., Cukrovarnická 10, 162 53 Praha 6, Czech Republic, and Institute of Physics, Johannes Gutenberg University, Staudinger Weg 7, 55128 Mainz, Germany

**K.V.** Karel Výborny, Institute of Physics ASCR, v.v.i., Cukrovarnická 10, 162 53 Praha 6, Czech Republic

**E.K.V.** Erin K. Vehstedt, Department of Physics, Texas A&M University, College Station, Texas 77843-4242, USA and Institute of Physics ASCR, v.v.i., Cukrovarnická 10, 162 53 Praha 6, Czech Republic

**J.W.** Joerg Wunderlich, Institute of Physics ASCR, v.v.i., Cukrovarnická 10, 162 53 Praha 6, Czech Republic and Hitachi Cambridge Laboratory, Cambridge CB3 0HE, United Kingdom

**L.P.Z.** Liviu P. Zârbo, Institute of Physics ASCR, v.v.i., Cukrovarnická 10, 162 53 Praha 6, Czech Republic